

The trap in the early Universe: impact on the interplay between gravitational waves and LHC physics in the 2HDM

Thomas Biekötter^{1§}, Sven Heinemeyer^{2¶}, José Miguel No^{2,3||},
María Olalla Olea-Romacho^{1**} and Georg Weiglein^{1,4††}

¹*Deutsches Elektronen-Synchrotron DESY, Notkestr. 85, 22607 Hamburg, Germany*

²*Instituto de Física Teórica UAM-CSIC, Cantoblanco, 28049, Madrid, Spain*

³*Departamento de Física Teórica, Universidad Autónoma de Madrid (UAM),
Campus de Cantoblanco, 28049 Madrid, Spain*

⁴*II. Institut für Theoretische Physik, Universität Hamburg, Luruper Chaussee 149,
22761 Hamburg, Germany*

Abstract

We analyze the thermal history of the 2HDM and determine the parameter regions featuring a first-order electroweak phase transition (FOEWPT) and also much less studied phenomena like high-temperature electroweak (EW) symmetry non-restoration and the possibility of vacuum trapping (i.e. the Universe remains trapped in an EW-symmetric vacuum throughout the cosmological evolution, despite at $T = 0$ the EW breaking vacuum is deeper). We show that the presence of vacuum trapping impedes a first-order EW phase transition in 2HDM parameter-space regions previously considered suitable for the realization of electroweak baryogenesis. Focusing then on the regions that do feature such a first-order transition, we show that the 2HDM parameter space that would yield a stochastic gravitational wave signal potentially detectable by the future LISA observatory is very contrived, and will be well probed by direct searches of 2HDM Higgs bosons at the HL-LHC, and (possibly) also via measurements of the self-coupling of the Higgs boson at 125 GeV. This has an important impact on the interplay between LISA and the LHC regarding the exploration of first-order phase transition scenarios in the 2HDM: the absence of new physics indications at the HL-LHC would severely limit the prospects of a detection by LISA. Finally, we demonstrate that as a consequence of the predicted enhancement of the self-coupling of the Higgs boson at 125 GeV the ILC would be able to probe the majority of the 2HDM parameter space yielding a FOEWPT through measurements of the self-coupling, with a large improvement in precision with respect to the HL-LHC.

[§]thomas.biekoetter@desy.de

[¶]Sven.Heinemeyer@cern.ch

^{||}josemiguel.no@uam.es

^{**}maria.olalla.olea.romacho@desy.de

^{††}georg.weiglein@desy.de

Contents

1	Introduction	2
2	The Higgs sector of the 2HDM	4
2.1	Model definition and notation	4
2.2	2HDM effective potential and renormalization conditions	5
2.3	Scale dependence and perturbativity of scalar couplings	7
3	Thermal effects and thermal evolution	7
3.1	Finite-temperature effective potential	7
3.2	Characterization of first-order phase transitions	8
3.3	Vacuum trapping	10
3.4	EW symmetry non-restoration	10
3.5	Gravitational waves	11
4	2HDM thermal history and phenomenological implications	13
4.1	The cosmological evolution of the vacuum in the 2HDM	14
4.2	Phenomenological consequences of vacuum trapping	19
4.2.1	Implications for electroweak baryogenesis	19
4.2.2	Gravitational waves	22
4.3	Interplay between the HL-LHC (and beyond) and LISA	28
4.3.1	GWs at LISA vs. direct BSM searches at the LHC	28
4.3.2	GWs at LISA vs. Higgs boson self-coupling measurements at LHC and ILC	30
5	Conclusions	34
A	Comparison of the renormalization scale dependence with changes of the 2HDM parameters	36

1 Introduction

The discovery of a Higgs boson at about 125 GeV at the Large Hadron Collider (LHC) [1, 2] was a milestone in our understanding of the laws of nature. At present, the properties of the detected Higgs boson agree well with the predictions of the Standard Model (SM) [3, 4], but at the current $\sim 10\%$ precision of the Higgs boson signal strength measurements at the LHC the experimental results are also in agreement with a plethora of extensions of the SM. Such extensions could address the various shortcomings of the SM. In particular, the ingredients of the SM are not sufficient to generate the observed matter-antimatter asymmetry of the Universe, the so-called *baryon asymmetry of the Universe* (BAU) [5–8].

It is well-known that the possible existence of extra Higgs doublets beyond the SM [9–11] could allow for the generation of the BAU via electroweak (EW) baryogenesis [12–15] (see [16–18] for general reviews on EW baryogenesis). Such a scenario requires a (strong) first order EW phase transition (FOEWPT), which provides the required out-of-equilibrium conditions for baryogenesis in the early Universe [19]. Scenarios featuring a FOEWPT also have the remarkable feature that they would lead to a stochastic gravitational wave (GW) background that could potentially be

detectable with future space-based gravitational wave observatories like the Laser Interferometer Space Antenna (LISA) [20, 21].

Theories with extended (non-minimal) Higgs sectors may also feature a rich variety of possible cosmological histories of the EW vacuum, as compared to the SM. In the SM the spontaneously broken EW symmetry is restored at high temperatures. The EW gauge symmetry is broken dynamically when the Universe cools down, which in the SM happens (for the measured Higgs boson mass $m_h \approx 125$ GeV) via a smooth cross-over transition [8]. It was however established long ago [22] that theories with additional scalar fields can give rise to different symmetry-breaking patterns as a function of the temperature of the Universe: a symmetry might remain broken at all temperatures, only be restored in an intermediate temperature region, or even be broken *only* at high temperatures, being unbroken at zero temperature. All these alternatives, so-called “symmetry non-restoration” (SnR) scenarios, may occur for non-minimal Higgs sectors, with a potential impact on the viability of the “vanilla” EW baryogenesis mechanism. A further possibility in the thermal history of extended Higgs sectors is vacuum trapping: at zero temperature the EW vacuum would exist as the deepest (or sufficiently long-lived) vacuum of the potential, but during the thermal evolution of the Universe the conditions for the on-set of the EW phase transition would never be fulfilled. Thus, the Universe would remain trapped in a (higher-energetic) non-EW vacuum, yielding an unphysical scenario. Parameter regions giving rise to vacuum trapping can therefore be excluded [23–25].

In this work we analyze in detail the thermal history of the Universe in the two-Higgs-doublet model (2HDM) (see Ref. [26] for a review). In particular, we investigate the occurrence of a FOEWPT as needed for EW baryogenesis, as well as the production of GWs potentially observable by LISA. We show the important impact that SnR and vacuum-trapping phenomena (which can appear in the 2HDM despite its relatively simple structure) have in shaping the 2HDM regions of parameter space where baryogenesis and/or GW production are possible. In particular, we demonstrate that vacuum-trapping reduces the 2HDM parameter range for which a GW signal from a FOEWPT would be observable by LISA to a very fine-tuned parameter-space region.

In addition, focusing on the type II 2HDM, we investigate the connection between the thermal history of the early Universe, particularly regarding a possible FOEWPT, and phenomenological signatures at colliders (see Refs. [27–32] for earlier analyses of this connection in the 2HDM): we study the new BSM Higgs boson signatures that are favored by scenarios with a FOEWPT. We demonstrate that ongoing and future LHC searches in final states with top quarks will probe the vast majority of the 2HDM parameter-space region yielding a strongly FOEWPT, already covering the entire region accessible via GW observations by LISA. We also analyze the connection between a FOEWPT and a large enhancement of the self-coupling of the Higgs boson at 125 GeV with respect to its SM value [33, 34]. We show that experimental information on the Higgs boson self-coupling at the High-Luminosity (HL)-LHC and particularly at the International Linear Collider (ILC) will provide a very promising route for probing FOEWPT scenarios in the 2HDM (and more broadly, in extended Higgs sectors).

Our work is organized as follows: In section 2 we discuss the Higgs sector of the 2HDM including higher-order corrections. The effects of the thermal (early universe) evolution of the EW vacuum are reviewed in section 3, where we also discuss the general aspects of SnR, vacuum trapping, and GW production during a FOEWPT. Our analysis of the cosmological evolution of the scalar vacuum in different regions of the 2HDM parameter space is then presented in section 4, and the connection with both GW production and collider phenomenology is discussed, providing a critical view on the interplay between these two. Our conclusions can be found in section 5.

2 The Higgs sector of the 2HDM

In this section we discuss the aspects of the 2HDM that are relevant for this work: we first briefly review the CP-conserving 2HDM with a softly broken \mathbb{Z}_2 symmetry (see e.g. Ref. [26] for further details) and specify our notation and conventions; we then discuss the theoretical and experimental constraints that shape the allowed parameter space of the model, before describing the form of the one-loop effective potential and the renormalization group running of 2HDM scalar couplings.

2.1 Model definition and notation

The tree-level potential of the CP-conserving 2HDM with a softly-broken \mathbb{Z}_2 symmetry is given by

$$V_{\text{tree}} = m_{11}^2 |\Phi_1|^2 + m_{22}^2 |\Phi_2|^2 - m_{12}^2 (\Phi_1^\dagger \Phi_2 + \text{h.c.}) + \frac{\lambda_1}{2} (\Phi_1^\dagger \Phi_1)^2 + \frac{\lambda_2}{2} (\Phi_2^\dagger \Phi_2)^2 + \lambda_3 (\Phi_1^\dagger \Phi_1) (\Phi_2^\dagger \Phi_2) + \lambda_4 (\Phi_1^\dagger \Phi_2) (\Phi_2^\dagger \Phi_1) + \frac{\lambda_5}{2} \left[(\Phi_1^\dagger \Phi_2)^2 + \text{h.c.} \right], \quad (1)$$

where all the parameters are real as a result of hermiticity and CP-conservation. The \mathbb{Z}_2 symmetry in (1), $\Phi_1 \rightarrow \Phi_1$, $\Phi_2 \rightarrow -\Phi_2$ is broken softly by the m_{12}^2 term. We expand the fields around the EW minimum as follows,

$$\Phi_1 = \begin{pmatrix} \phi_1^+ \\ (v_1 + \rho_1 + i\sigma_1)/\sqrt{2} \end{pmatrix}, \quad \Phi_2 = \begin{pmatrix} \phi_2^+ \\ (v_2 + \rho_2 + i\sigma_2)/\sqrt{2} \end{pmatrix}, \quad (2)$$

where v_1 and v_2 are the field vevs for the two Higgs doublets (at zero temperature), and the EW scale is defined as $v = \sqrt{v_1^2 + v_2^2} \approx 246$ GeV. After spontaneous symmetry breaking, the CP-conserving 2HDM gives rise to five physical mass eigenstates in the scalar sector: two CP-even neutral scalars h and H , one CP-odd neutral pseudoscalar A and a pair of charged states H^\pm . In addition, there are one neutral and two charged massless Goldstone bosons, G^0 and G^\pm respectively, which are absorbed into longitudinal polarisations of the gauge bosons Z and W^\pm , respectively.

For the CP-odd and the charged scalar sectors, the mass eigenstates are related to the gauge eigenstates by an orthogonal rotation by the angle β , defined as $t_\beta \equiv \tan \beta = v_2/v_1$. For the CP-even sector, the mixing angle α can be treated as a free parameter. The parameters α and β control the coupling strength of the scalar particles to fermions and gauge bosons (see e.g. Ref. [26] for the explicit form of the effective couplings). Therefore, it is convenient to perform our analysis in terms of the particle masses of the Higgs sector and the mixing angles since their phenomenological impact is transparent. We choose the following set of independent parameters:

$$t_\beta, m_{12}^2, v, \cos(\beta - \alpha), m_h, m_H, m_A, m_{H^\pm}. \quad (3)$$

Here, m_h and m_H are the masses of the CP-even Higgs bosons, m_A is the mass of the CP-odd Higgs boson, and m_{H^\pm} is the mass of the charged Higgs bosons, respectively. The parameter $\cos(\alpha - \beta)$ is chosen in order to have a measure as to how closely the state h , which in the following plays the role of the discovered Higgs boson at $m_h \approx 125$ GeV, resembles the properties of a SM Higgs boson. In the so-called alignment limit [35] $\cos(\alpha - \beta) = 0$, the lowest-order couplings of h to the SM particles are precisely as predicted by the SM, whereas $\cos(\alpha - \beta) \neq 0$ gives rise to deviations

of the couplings of h from their SM values. The relations between the set of input parameters shown in Eq. (3) and the Lagrangian parameters shown in Eq. (1) can be found in Ref. [26].

The \mathbb{Z}_2 symmetry in Eq. (1) is extended to the Yukawa sector of the theory in order to avoid tree-level flavour-changing neutral currents (FCNCs): as the two fields Φ_1 and Φ_2 transform differently under the \mathbb{Z}_2 symmetry, they cannot be coupled both to the same SM fermions, leading to the absence of tree-level FCNCs. There are four 2HDM configurations/types that avoid FCNCs at tree-level, characterized by the \mathbb{Z}_2 charge assignment of the fermion fields in the Yukawa sector. As a consequence, in addition to the values of the free parameters shown in Eq. (3) the Yukawa type of the 2HDM has to be specified. Here we will concentrate on the 2HDM of type II, and focus on the alignment limit.

The parameter space of the CP-conserving 2HDM, which has eight independent parameters as specified above, is restricted by various experimental and theoretical constraints. To implement these in our analysis, we make use of several public codes. We scan the 2HDM parameter space with the code `ScannerS` [36, 37] in terms of the set of parameters shown in Eq. (3). `ScannerS` checks whether the parameter point under investigation is in agreement with perturbative unitarity, boundedness from below and vacuum stability at zero temperature. Concerning the experimental constraints, `ScannerS` also ensures that a parameter point is in agreement with bounds coming from flavour-physics observables [38] and electroweak precision observables (EWPO) [38–40].¹ In addition, we make use of `HiggsSignals` [42–45] and `HiggsBounds` [46–50] to incorporate bounds from measurements of the properties of the experimentally detected Higgs boson at about 125 GeV and searches for additional scalar states, respectively. The required cross sections and branching ratios of the scalars have been obtained with the help of `SusHi` [51] and `M2HDECAY` [52], respectively.

2.2 2HDM effective potential and renormalization conditions

The zero-temperature effective potential (see e.g. Ref. [53] for a review) includes the effect of radiative corrections into the scalar potential of the theory. At one-loop, the effective potential V_{eff} for the 2HDM is given by

$$V_{\text{eff}} = V_{\text{tree}} + V_{\text{CW}} + V_{\text{CT}}, \quad (4)$$

where V_{tree} is the 2HDM tree-level potential given in Eq. (1), V_{CW} represents the one-loop radiative corrections in the form of the Coleman-Weinberg potential [54], and V_{CT} contains UV-finite counterterm contributions that are specified below. V_{CW} is given in the $\overline{\text{MS}}$ renormalization scheme by

$$V_{\text{CW}}(\phi_i) = \sum_j \frac{n_j}{64\pi^2} (-1)^{2s_j} m_j(\phi_i)^4 \left[\ln \left(\frac{|m_j(\phi_i)|^2}{\mu^2} \right) - c_j \right], \quad (5)$$

where $m_j(\phi_i)$ are the field-dependent tree-level masses, s_j the particle spins and n_j the corresponding numbers of degrees of freedom. The constants c_j arise from the $\overline{\text{MS}}$ renormalization prescription, with $c_j = 5/6$ for gauge bosons and $c_j = 3/2$ for scalars and fermions. We set the renormalization scale μ to be equal to the SM EW vev, $\mu = v$. In the 2HDM, the sum in Eq. (5) runs over the neutral scalars $\Phi^0 = \{h, H, A, G^0\}$, the charged scalars $\Phi^\pm = \{H^\pm, G^\pm\}$, the longitudinal and transversal gauge bosons, $V_L = \{Z_L, W_L^+, W_L^-\}$ and $V_T = \{Z_T, W_T^+, W_T^-\}$ and the

¹The check for the agreement with the EWPO (carried out on the basis of the oblique parameters) does not take into account the new measurement of the W -boson mass reported recently by the CDF collaboration [41], which is in significant tension with the SM predictions.

SM quarks q and leptons ℓ . The degrees of freedom n_j for the species of each type are

$$n_{\Phi^0} = 1, \quad n_{\Phi^\pm} = 2, \quad n_{V_T} = 2, \quad n_{V_L} = 1, \quad n_q = 12, \quad n_\ell = 4.$$

The omission of ghost contributions is due to the choice of evaluating the Coleman-Weinberg potential in the Landau gauge.²

In order to simplify our analysis, we require the zero-temperature loop-corrected vacuum expectation values, scalar masses and mixing angles to be equal to their tree-level values, and we refer to this prescription as “on-shell” (OS) renormalization in the remainder of the paper. To achieve this, we add a set of UV-finite counterterms V_{CT} to the effective potential, given by

$$V_{\text{CT}} = \sum_i \frac{\partial V_0}{\partial p_i} \delta p_i, \quad (6)$$

where the p_i denote the parameters of the tree-level potential. In order to fulfill the conditions mentioned above, V_{CT} is required to satisfy the following renormalization conditions,

$$\partial_{\phi_i} V_{\text{CT}}(\phi) \Big|_{\langle\phi\rangle_{T=0}} = -\partial_{\phi_i} V_{\text{CW}}(\phi) \Big|_{\langle\phi\rangle_{T=0}}, \quad (7)$$

$$\partial_{\phi_i} \partial_{\phi_j} V_{\text{CT}}(\phi) \Big|_{\langle\phi\rangle_{T=0}} = -\partial_{\phi_i} \partial_{\phi_j} V_{\text{CW}}(\phi) \Big|_{\langle\phi\rangle_{T=0}}, \quad (8)$$

where $\langle\phi\rangle_{T=0}$ corresponds to the tree-level vacuum configuration at zero temperature. To compute the finite set of counterterms, we made use of the public code BSMPT [59, 60].

The effective potential explicitly depends on the renormalization scale μ . As mentioned above, in our numerical analysis this scale was set equal to v , which is the relevant energy scale for the physics at the EW scale. Although the OS prescription discussed above gives rise to a partial cancellation of the renormalization scale dependence, there still remains a dependence on μ for the quantities that describe the EW phase transition, in particular once the thermal effects are taken into account (see Sect. 3). For a single parameter point, the residual scale dependence is relevant for the prediction of parameters like the transition strengths or the SNR of the associated GW signal, where the predicted values can vary substantially for different choices of μ [61]. However, the logarithmic μ -dependence (see Eq. (5)) is much milder compared to the dependence on the 2HDM model parameters (such as the masses of the BSM Higgs bosons). As a result, changes in the predictions for the EW phase transition arising from a modification of μ can be compensated by very small changes of the model parameters. Given the fact that BSM theories like the 2HDM have several free parameters, in our phenomenological analysis we are mainly interested in identifying regions of the 2HDM parameter space that are suitable for the realization of EW SnR, a strong FOEWPT and observable GW signals. As will be discussed in the numerical analysis, the shapes and sizes of these regions are very sensitive to a variation of the 2HDM model parameters. Since the renormalization scale dependence is much milder, the qualitative distinction between the different parameter regions is only marginally affected by variations of μ . Therefore, also our conclusions about the interplay between the possibility of a detection of GWs and the physics at the LHC in the context of the 2HDM are not significantly affected by the renormalization-scale dependence. In order to illustrate this point in more detail, we supplement our numerical discussion with a comparison of the μ -dependence with the dependence on the model parameters for an example scenario in App. A.

²Discussions on the gauge dependence of the effective potential in the context of the electroweak phase transition can be found in Refs. [55–58].

2.3 Scale dependence and perturbativity of scalar couplings

The renormalization group evolution of the quartic scalar couplings λ_i can provide significant constraints on the viable region of the 2HDM parameter space. Even if $\lambda_i(\mu)$ are perturbative at an energy scale $\mu = v$, the running of the parameters may drive the 2HDM quartic couplings into a non-perturbative regime. Depending on the values of $\lambda_i(v)$ this can happen already at relatively low energy scales (i.e. not far from the EW scale). Hence, as an important ingredient of our analysis, we solve the renormalization group equations (RGEs) for the model parameter points discussed, and require that the $\lambda_i(\mu)$ remain below the perturbativity bound 4π for any value of the energy scale μ up to the physical scalar masses of the theory m_j , i.e. $\lambda_i(\mu) < 4\pi$ for $\mu \leq m_j$ ($\forall j$). This provides a (minimal) theoretical consistency condition on the 2HDM parameter space in relation to renormalization group evolution.

We have numerically solved the RGEs taking into account the one-loop and two-loop contributions to the β -functions of the model parameters computed with the help of the public code `2HDME` [62]. In order to obtain $\overline{\text{MS}}$ parameters $p^{\overline{\text{MS}}}$ (as required by `2HDME`) from our OS parameters p^{OS} , we transformed the parameters according to

$$p^{\text{OS}}(\mu_0) + \delta p^{\text{OS}}(\mu_0) = p^{\overline{\text{MS}}}(\mu_0) + \delta p^{\overline{\text{MS}}}(\mu_0) \quad (9)$$

$$\Rightarrow p^{\overline{\text{MS}}}(\mu_0) = p^{\text{OS}}(\mu_0) + \delta p(\mu_0) , \quad (10)$$

where $\delta p^{\overline{\text{MS}}}$ are the parameter counterterms in the $\overline{\text{MS}}$ scheme (consisting only of a UV-divergent contribution), and $\delta p^{\text{OS}} = \delta p^{\overline{\text{MS}}} + \delta p$ are the OS counterterms that additionally contain the UV-finite shifts δp introduced in Eq. (6). We also stress that thermal effects, to be discussed in the next section, introduce the temperature of the system T as a relevant energy scale. Then, for the study of the scalar potential at temperatures substantially larger than the EW scale, $T \gg v$ (targeted towards the investigation of whether the EW symmetry is restored for high temperatures, see section 3.4), we must also require $\lambda_i(\mu = T)$ to be perturbative.

3 Thermal effects and thermal evolution

We now describe the addition of thermal corrections to the effective potential V_{eff} , which allows the extension of the analysis of vacuum configurations to finite temperatures. Subsequently, we discuss several phenomena which may occur in the thermal evolution of the vacuum configuration of a (multi-) Higgs potential: a first-order EW phase transition, possibly with an accompanying stochastic signal of gravitational waves (GW); the non-restoration of EW symmetry at high temperatures (see [25, 63]); and the trapping of the vacuum in an unbroken EW configuration (see [24, 25]). In this section we give general details of our computational set-up for these phenomena, and analyze their impact on the 2HDM parameter space in section 4.

3.1 Finite-temperature effective potential

At finite temperature T , the one-loop effective potential from Eq. (4) receives thermal corrections V_T , given by [53, 55]

$$V_T(\phi_i) = \sum_j \frac{n_j T^4}{2\pi^2} J_{\pm} \left(\frac{m_j^2(\phi_i)}{T^2} \right), \quad (11)$$

where the thermal integrals J_- for bosons and J_+ for fermions, respectively, are defined by

$$J_{\pm} \left(\frac{m_j^2(\phi_i)}{T^2} \right) = \mp \int_0^{\infty} dx x^2 \log \left[1 \pm \exp \left(-\sqrt{x^2 + \frac{m_j^2(\phi_i)}{T^2}} \right) \right]. \quad (12)$$

Besides the degrees of freedom considered in Eq. (5), the sum in Eq. (11) includes the photon, which acquires an effective thermal mass at finite temperature (and therefore must be included in the sum of Eq. (11) in spite of being massless at $T = 0$).

In addition, the breakdown of the fixed-order result of the perturbative expansion in the high-temperature limit is a well-known problem of finite-temperature field theory. It can be addressed through the resummation of a certain set of higher-loop diagrams [64–66], the so-called daisy contributions (see Ref. [53] for a review). There are various daisy-resummation prescriptions in the literature.³ We here follow the Arnold-Espinosa method [66], which amounts to resumming the infrared-divergent contributions from the bosonic Matsubara zero-modes by adding the additional contribution V_{daisy} to the one-loop effective potential at finite temperature. V_{daisy} is given by

$$V_{\text{daisy}} = - \sum_k \frac{T}{12\pi} \left((\bar{m}_k^2(\phi))^{\frac{3}{2}} - (m_k^2(\phi))^{\frac{3}{2}} \right), \quad (13)$$

where the sum in k runs over the bosonic degrees of freedom yielding infrared-divergent contributions, and \bar{m}_k^2 denotes their corresponding squared thermal masses [68], which have been obtained as in Ref. [29]. In the 2HDM, the sum in k runs over all the fields $\phi \in \{\Phi^0, \Phi^{\pm}, V_L, \gamma_L\}$, where γ_L is the longitudinal polarisation of the photon, which acquires a mass at finite temperature.

With the inclusion of thermal corrections, the 2HDM (finite-temperature) one-loop effective potential with daisy-resummation reads

$$V_{\text{eff}} = V_{\text{tree}} + V_{\text{CW}} + V_{\text{CT}} + V_{\text{T}} + V_{\text{daisy}}. \quad (14)$$

with V_{tree} , V_{CW} and V_{CT} given in section 2, and V_{T} , V_{daisy} described above.

3.2 Characterization of first-order phase transitions

In this section we briefly review the analysis of the thermal evolution of the effective potential V_{eff} , for which we use the public code `CosmoTransitions` [69]). We are particularly interested in the occurrence of a first-order EW phase transition (FOEWPT), which requires the coexistence (at some temperature in the early Universe) of the EW minimum and another minimum. At the critical temperature T_c these two minima are degenerate, while for $T < T_c$, the EW minimum has lower energy than the other (metastable) vacuum. In this case, the occurrence of the FOEWPT depends on the transition rate per unit time and unit volume for the phase transition from the metastable or false vacuum into the true (EW) vacuum [70–73],

$$\Gamma(T) = A(T) e^{-S_3(T)/T}, \quad (15)$$

³See [25] for a comparison between the Arnold-Espinosa and the Parwani resummation methods. Recent computations of the characteristics of first-order phase transitions that go beyond the usual daisy-resummed approach have been performed, for instance, in Refs. [61, 67], where it was shown that two-loop contributions to the effective potential can be sizable. We leave a discussion of the 2HDM potential beyond the one-loop level for future studies.

where S_3 denotes the three-dimensional action for the “bounce” (multi-)field configuration ϕ_B that interpolates between the metastable and EW vacua for $T < T_c$,

$$S_3(T) = 4\pi \int r^2 dr \left[\frac{1}{2} \left(\frac{d\phi_B}{dr} \right)^2 + V_{\text{eff}}(\phi_B, T) \right]. \quad (16)$$

Specifically, the bounce ϕ_B is the configuration of scalar fields ϕ that solves the equations of motion derived from the action (16) with boundary conditions $d\phi/dr|_{r=0} = 0$ and approaching the false vacuum at $r \rightarrow \infty$. Physically, ϕ_B describes a bubble of the true vacuum phase nucleating in the false vacuum background. The prefactor $A(T)$ is a functional determinant [71] given approximately by $A(T) \sim T^4 (S_3/2\pi T)^{3/2}$ [72]. The onset of the FOEWPT occurs when the time integral of the transition rate (15) within a Hubble volume H becomes of order one. This defines the nucleation temperature T_n (see e.g. [74]) as

$$\int_{T_n}^{T_c} \frac{T^4}{H^4} \frac{A(T)}{T} e^{-S_3(T)/T} dT \sim 1, \quad (17)$$

where we have used the time-temperature relation in an expanding Universe assumed to be dominated by radiation. The Hubble parameter H is given by $H^2 = (8\pi^3 g_{\text{eff}}(T) T^4)/(90 M_{\text{Pl}}^2)$, with $g_{\text{eff}}(T)$ the effective number of relativistic degrees of freedom at a temperature T and $M_{\text{Pl}} = 1.22 \times 10^{19}$ GeV the Planck mass. Eq. (17) roughly yields [21]

$$S_3(T_n)/T_n \sim 140, \quad (18)$$

as the requirement for the occurrence of a FOEWPT. The possibility that the condition (17) is not satisfied for any temperature below the critical temperature T_c will be discussed in section 3.3.

On general grounds, a cosmological first-order phase transition can be characterized by four macroscopic parameters which we specify in the following. These parameters are obtained from the microscopic properties of the underlying particle physics model, in our case the 2HDM. As will be discussed in more detail in section 3.5, these parameters also determine the predictions of the amplitude and the spectral shape of the stochastic GW background that is generated during the first-order phase transition.

The first key parameter is the temperature T_* at which the phase transition takes place. The second parameter, α , measures the strength of the phase transition. Following Refs. [20, 21], we define α as the difference of the trace of the energy-momentum tensor between the two (false and true vacua) phases, normalised to the radiation background energy density, i.e.

$$\alpha = \frac{1}{\rho_R} \left(\Delta V(T_*) - \left(\frac{T}{4} \frac{\partial \Delta V(T)}{\partial T} \right) \Big|_{T_*} \right). \quad (19)$$

Here $\Delta V(T) = V_f - V_t$, with $V_f \equiv V_{\text{eff}}(\phi_f)$ and $V_t \equiv V_{\text{eff}}(\phi_t)$ being the values of the potential in the false and the true vacuum, respectively.⁴ ρ_R is the background energy density assuming a radiation dominated Universe, i.e. $\rho_R = \pi^2 g_{\text{eff}}(T_*) T_*^4/30$. We also note that for cosmological phase

⁴In some studies (see, for instance, Refs. [32, 75] for 2HDM analyses) the parameter α has been defined instead as the latent heat released during the transition divided by ρ_R , in which case the factor 1/4 in the second term in Eq. (19) is absent. However, recent studies have shown that the definition used here yields a better description of the energy budget available for the production of GW waves compared to a definition of α by means of the pressure difference or the energy difference [76].

transitions which are not very strong, i.e. $\alpha \ll 1$, the transition temperature T_* can be identified with the nucleation temperature T_n defined by Eq. (17) [20], since the temperature at the onset of the transition is approximately equal to the temperature for which true vacuum bubbles collide and the phase transition completes.

The third quantity is the inverse duration of the phase transition in Hubble units, β/H . It can generally be expressed (see [77] for a discussion) in terms of the derivative of the action S_3 with respect to the temperature evaluated at the time of the phase transition,

$$\frac{\beta}{H} = T_* \left(\frac{d}{dT} \frac{S_3(T)}{T} \right) \Big|_{T_*}. \quad (20)$$

The fourth quantity that characterizes a cosmological first-order phase transition is the bubble wall velocity v_w . So far, except for the case of ultrarelativistic bubbles [78, 79] the computation of v_w is generally a very complicated task that requires solving a coupled system of Boltzmann and scalar field equations in a fairly model-dependent approach (see Refs. [80–89], as well as [20, 21] for a general discussion). There is no precise prediction for v_w in the 2HDM (or related extensions of the SM) available in the literature.⁵ Hence, we will treat v_w as a free parameter in our analysis (see also the discussion in section 3.5).

3.3 Vacuum trapping

If the condition (17) is not met for any temperature below T_c , the Universe would remain stuck in a false vacuum in spite of the existence of a deeper EW symmetry-breaking minimum of the potential at zero temperature. This phenomenon is dubbed “vacuum trapping”. In particular, when aiming to identify the parameter-space regions of a BSM model where a FOEWPT occurs, the possibility of vacuum trapping highlights that an approach based solely on the critical temperature T_c is not sufficient and may yield misleading results. Vacuum trapping has been recently discussed in the context of the N2HDM [25] and the NMSSM [24] and also previously in the context of color-breaking minima within the MSSM [23]. In the 2HDM, vacuum trapping has been very recently explored in Ref. [32], emphasizing that this phenomenon may take place in particular if the barrier between the false and the true vacua is driven almost exclusively by the radiative corrections, rather than by the thermal contributions to the effective potential.

3.4 EW symmetry non-restoration

It is known that in certain extensions of the SM the EW symmetry can be broken already at temperatures much larger than the EW scale, resulting in EW symmetry non-restoration (SnR) [25, 63, 90–95]. The effect of SnR can exist up to possibly very high temperatures, and it is also possible to find no restoration at all within the energy range in which the model under consideration is theoretically well-defined. As it has been discussed in Ref. [25] for the 2HDM extended with a real singlet field (N2HDM), in extensions of the SM by a second Higgs doublet the presence of EW SnR is related to the existence of sizeable quartic scalar couplings and the impact of the resummation of infrared divergent modes in the scalar potential. In that scenario, the maximum temperature up to which the analysis of SnR is valid corresponds to the upper cut-off $\Lambda_{4\pi}$ defined

⁵See Ref. [15] for estimates of v_w in the 2HDM for some special parameter configurations. A simple analytical formula to predict v_w has been found in Ref. [88]. However, this formula has not yet been applied to models with a second Higgs doublet and it is unclear how accurate the prediction for v_w would be for the 2HDM.

as the energy scale μ at which one of the quartic couplings reaches the naive perturbative bound 4π . $\Lambda_{4\pi}$ is representative of the energy scale μ at which the theory enters a non-perturbative regime. In section 4 we will demonstrate that EW SnR is possible within the 2HDM, and that SnR appears in regions of the parameter space adjacent to those where a FOEWPT is present. We will also discuss the consequences of EW SnR with regards to the viability of a parameter point taking into account the thermal history of the Higgs vacuum, and we briefly comment on the phenomenological implications.⁶

3.5 Gravitational waves

Cosmological first-order phase transitions provide a particularly compelling possibility for the generation of GWs in the early Universe. The collisions of the expanding bubbles and the resulting motion of the ambient cosmic fluid source a stochastic GW background that could be observable at future GW interferometers (see e.g. Refs. [20, 21, 96] for a discussion). For FOEWPTs in the 2HDM, where the expanding bubbles do not run-away [15], the contribution from the bubble collisions themselves can be safely neglected. Then, GWs are generated from the sound waves and turbulence generated in the plasma following the bubble collisions [20]. As introduced in section 3.2 the GW spectrum produced in a FOEWPT is characterized by four essential quantities [20, 21]: the transition temperature T_* , the strength α , the inverse duration of the phase transition β/H , and the bubble wall velocity v_w , i.e. the speed of the bubble wall after nucleation in the rest frame of the plasma far away from the phase-transition interface. The GW power spectrum as a function of frequency $h^2\Omega_{\text{GW}}(f)$ is given by

$$h^2\Omega_{\text{GW}}(f) = h^2\Omega_{\text{sw}}(f) + h^2\Omega_{\text{turb}}(f) , \quad (21)$$

where $h^2\Omega_{\text{sw}}$ and $h^2\Omega_{\text{turb}}$ are the contributions from sound waves and turbulence, respectively. The contribution from sound waves propagating in the plasma was originally obtained with the help of large-scale lattice simulations of bubble collisions inducing bulk fluid motion [97, 98]. It can be written as [20] (see also [99, 100])

$$\Omega_{\text{sw}}(f) = 0.687 F_{\text{gw},0} \Gamma^2 \bar{U}_f^4 \left(\frac{H_* R_*}{c_s} \right) \tilde{\Omega}_{\text{gw}} \left(\frac{H_* \tau_{\text{sw}}}{c_s} \right) C(f/f_{\text{sw,p}}) , \quad (22)$$

with

$$F_{\text{gw},0} = 3.57 \cdot 10^{-5} \left(\frac{100}{g_*} \right)^{1/3} , \quad \tilde{\Omega}_{\text{gw}} = 0.012 . \quad (23)$$

We have also introduced the speed of sound of a relativistic plasma $c_s = 1/\sqrt{3}$ and the adiabatic index $\Gamma = 4/3$. \bar{U}_f is the the root-mean-square four-velocity of the plasma given by

$$\bar{U}_f^2 = \frac{\kappa\alpha}{\Gamma(1+\alpha)} , \quad (24)$$

where κ denotes the efficiency factor (i.e. the relevant energy fraction for sound waves), which is a function of α and v_w that also depends on the steady-state bubble expansion regime (deflagrations,

⁶We make use here of the numerical treatment of the finite-temperature one-loop effective potential. For a detailed analytical discussion of SnR in the high-temperature limit we refer the reader to Ref. [25].

detonations or hybrids, see e.g. [101]), which we obtain following Ref. [101]. The mean bubble separation R_* entering (22) is defined by

$$H_* R_* = (8\pi)^{1/3} \left(\frac{\beta}{H} \right)^{-1} \max(v_w, c_s). \quad (25)$$

The factor $H_* \tau_{\text{sw}}$ in Eq. (22) is introduced in order to account for a timescale τ_{sh} for the formation of shocks in the plasma (leading to the damping of the sound waves) that may be shorter than one Hubble time [102]

$$H_* \tau_{\text{sw}} = \min(1, H_* \tau_{\text{sh}}) \quad \text{with} \quad H_* \tau_{\text{sh}} \simeq \frac{H_* R_*}{\bar{U}_f}. \quad (26)$$

Finally, the spectral shape of the sound-wave signal is approximated by the function

$$C(s) = s^3 \left(\frac{7}{4 + 3s^2} \right)^{7/2}, \quad (27)$$

and the associated peak frequency is given by

$$f_{\text{sw,p}} = 26 \left(\frac{1}{H_* R_*} \right) \left(\frac{T_*}{100 \text{ GeV}} \right) \left(\frac{g_*}{100} \right)^{1/6} \mu\text{Hz}. \quad (28)$$

As indicated above, if the sound-wave period is much shorter than a Hubble time ($H_* \tau_{\text{sw}} \ll 1$), a large fraction of the energy stored in the bulk motion of the plasma does not get to produce GW from sound waves. Yet, when the fluid flow becomes nonlinear (giving rise to shock formation), it can lead to the appearance of turbulence in the plasma, which in turn can also generate GWs. Following Ref. [102], we have modelled $h^2 \Omega_{\text{turb}}$ under the most optimistic assumption that all the energy remaining in the plasma when the sound waves are damped gets transformed into turbulence. In this case, the spectrum of GWs from turbulence may be written as [103]

$$\Omega_{\text{turb}} = 7.23 \cdot 10^{-4} \left(\frac{100}{g_*} \right)^{1/3} v_w \left(\frac{\beta}{H} \right)^{-1} (1 - H_* \tau_{\text{sw}}) \Gamma^{3/2} \bar{U}_f^3 D(f, f_{\text{turb,p}}), \quad (29)$$

with peak frequency

$$\frac{f_{\text{turb,p}}}{H_*} = 1.75 \left(\frac{\beta}{H} \right) \left(\frac{1}{\max(v_w, c_s)} \right) \mu\text{Hz}, \quad \text{with} \quad H_* = 1.65 \cdot 10^{-5} \left(\frac{T_*}{100 \text{ GeV}} \right) \left(\frac{g_*}{100} \right)^{1/6}, \quad (30)$$

and the spectral shape approximated by

$$D(f, f_p) = \left(\frac{f}{f_p} \right)^3 \left(1 + \frac{f}{f_p} \right)^{-11/3} \left(1 + 8\pi \frac{f}{H_*} \right)^{-1}. \quad (31)$$

We note in any case that the details of the GW spectrum produced from turbulence constitute a subject of ongoing debate (see e.g. Refs. [104–106]). At the same time, we have assumed for simplicity in this work that all the energy remaining in the plasma after the sound waves are switched off leads to turbulence. This gives rise to the factor $(1 - H_* \tau_{\text{sw}})$ in Eq. (29), to be compared with the factor $H_* \tau_{\text{sw}}$ in Eq. (22). We also stress that the efficiency of turbulence generation as a result of nonlinearities in the plasma is currently under investigation [107]. Nevertheless, we

here find that Ω_{turb} plays only a minor role in our estimate of the GW spectrum, since it has a substantially smaller peak amplitude compared to Ω_{sw} .⁷

The value of the EW scale is such that the GW signal from a FOEWPT would lie within the frequency sensitivity band of the future space-based LISA GW interferometer. In order to assess the detectability of a GW signal from a FOEWPT by LISA one has to evaluate the Signal-to-Noise Ratio (SNR) of the GWs. The SNR can be computed according to [20]

$$\text{SNR} = \sqrt{\mathcal{T} \int_{-\infty}^{+\infty} df \left[\frac{h^2 \Omega_{\text{GW}}(f)}{h^2 \Omega_{\text{Sens}}(f)} \right]^2}, \quad (32)$$

where \mathcal{T} is the duration of the mission times its duty cycle. We have used values for $\mathcal{T} = 3$ y and 7 y. $\Omega_{\text{Sens}}(f)$ is the nominal sensitivity of a given LISA configuration to stochastic sources⁸, obtained from the power spectral density $S_h(f)$

$$h^2 \Omega_{\text{Sens}}(f) = \frac{2\pi^2}{3H_0^2} f^3 S_h(f), \quad (33)$$

with $S_h(f)$ taken from the LISA mission requirements [109]. In order to be considered detectable, a GW signal should give rise to roughly $\text{SNR} \gtrsim 10$ [20]. It should be noted, however, that our model predictions for SNR suffer from sizable theoretical uncertainties. In particular, both the peak frequency and the maximum amplitude of the power spectrum Ω_{sw} depend on the bubble wall velocity v_w , for which no well-established model prediction is available even though there are promising recent proposals such as in Refs. [88, 89]. For most parts of our analysis, we will choose $v_w \simeq 0.6$, for which the best prospects regarding GW detection at LISA are obtained in the 2HDM (see section 4.3 for details).⁹ We nevertheless note that values of v_w largely different from 0.6 may give rise to substantially smaller SNR values at LISA. Thus, the predictions for the SNRs in our numerical discussion should be regarded as rough estimates.

4 2HDM thermal history and phenomenological implications

In this section we study the thermal history of the 2HDM regarding a FOEWPT and the associated production of GWs, as well as the occurrence of vacuum trapping and/or EW SnR. We analyze how these can yield interesting constraints on the parameter space of the 2HDM, and we discuss the potential complementarity between collider searches and GW probes with LISA.

The possibility of a FOEWPT in the CP-conserving 2HDM has been extensively studied (see Refs. [15, 32, 110] for analyses that include a calculation of the nucleation temperature). The usual scenario that features such a first-order transition requires relatively large quartic couplings,

⁷In particular, we find that including Ω_{turb} does not affect the SNR at LISA at the level of turning an undetectable GW signal into a detectable one. Still, for strong GW signals Ω_{turb} affects the overall GW spectral shape: as will be discussed in more detail in section 4.2, Ω_{turb} enhances the signal at the high-frequency tail, which leads to a slight increase in SNR (compared to the GW signal originated by Ω_{sw} alone) when the peak frequency of the sound wave contribution Ω_{sw} is lower than the frequency range for which LISA has the best sensitivity.

⁸When showing the LISA sensitivity curve in this work (e.g. in Fig. 4), it corresponds to the nominal LISA sensitivity $h^2 \Omega_{\text{Sens}}(f)$ rather than to the so-called power-law sensitivity of LISA [108] to cosmological sources.

⁹Remarkably, in Ref. [89] it has been found that for the values of α generically realized in the 2HDM, deflagration bubbles with $v_w \sim c_s$ (thus fairly close to our choice $v_w = 0.6$) are a relatively common feature of FOEWPTs, independently of the precise microscopic properties of the BSM model under consideration.

which subsequently implies sizeable splittings among the scalar masses and/or between these masses and the overall (squared) mass scale of the second doublet, $M^2 = m_{12}^2/s_\beta c_\beta$ [15, 28]. In this work we focus on the 2HDM with type-II Yukawas, for which stringent limits arising from flavor observables constrain the mass of the charged states to be $m_{H^\pm} \gtrsim 600$ GeV [38]. This requirement in conjunction with the constraints from electroweak precision observables favors the degeneracy of the masses of the heavy pseudoscalar and the charged scalar, $m_A \sim m_{H^\pm}$. In order to explore the parameter space of the 2HDM taking into account these considerations, we have scanned the parameter space of the CP-conserving type II 2HDM over the following ranges of the input parameters,

$$t_\beta = 3, \quad m_{h_1} = 125.09 \text{ GeV}, \quad 200 \text{ GeV} \leq m_H \leq 1 \text{ TeV},$$

$$600 \text{ GeV} \leq m_A = m_{H^\pm} \leq 1.2 \text{ TeV}, \quad \cos(\beta - \alpha) = 0, \quad M^2 = \frac{m_{12}^2}{s_\beta c_\beta} = m_H^2. \quad (34)$$

Using `ScannerS`, we have generated 10k 2HDM parameter points within the above ranges, passing all the theoretical and experimental constraints discussed in section 2.1. In a second step, we have analyzed the thermal history of each of these 10k benchmark points with `cosmoTransitions` [69], exploring the temperature range $[0, 700 \text{ GeV}]$. We have studied the temperature dependence of the minima of the one-loop effective potential V_{eff} from Eq. (14) in terms of the two CP-even neutral fields $(\rho_1(T), \rho_2(T))$. We then have computed the tunneling rate defined in Eq. (15) between coexisting minima at finite temperature, evaluating whether the criterion from Eq. (17) is met and a FOEWPT takes place.¹⁰

In section 4.1, we explore the different thermal histories that the CP-conserving 2HDM features within our parameter scan, which targets the regions where a FOEWPT is realized, as well as the vicinity of such regions. As mentioned before, a FOEWPT in the 2HDM strongly favours sizeable values of the quartic couplings, and we complement this analysis with a study of the energy scale dependence of the quartic couplings. We stress the rich variety of phenomena that arise within this parameter space region, and investigate in particular the effects of vacuum trapping and EW SnR. The analysis of the 2HDM thermal history will allow us to determine the regions of the parameter space in which the strongest FOEWPT can be realized in the type II 2HDM, and to assess how strong such transitions are. In section 4.2 we analyze the GW signals that are produced during the phase transitions. We will compare the predicted GW signals to the expected LISA sensitivity in order to assess whether such signals could be detectable at LISA. Finally, in section 4.3 we compare the prospects of a GW detection at LISA with the collider phenomenology of the corresponding 2HDM parameter regions in order to address the question whether those regions could also be probed in a complementary way by (HL-)LHC searches.

4.1 The cosmological evolution of the vacuum in the 2HDM

In this section we will investigate possible realizations of non-standard cosmological histories in the 2HDM. Even though the motivation for the analyzed parameter plane was its suitability for the occurrence of FOEWPTs, as described above, we point out that the considered parameter space also features a rich variety of thermal histories in terms of the patterns of symmetry breaking and symmetry restoration.

Before we start the discussion of the 2HDM cosmological history, we briefly inspect the additional constraints from the RGE running of the parameters, that we have applied in order to

¹⁰We do not take into account the possibility of CP-breaking or charge-breaking minima at finite temperature.

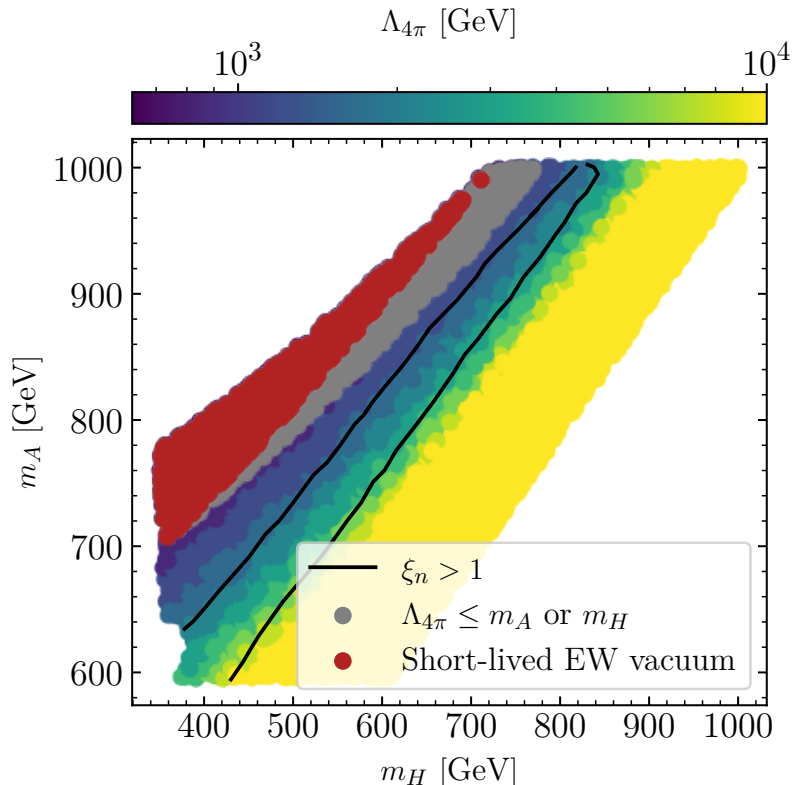


Figure 1: Constraints from perturbativity and vacuum stability, and region featuring a strong FOEWPT in the plane of the mass of the heavy CP-even scalar m_H and the masses of the CP-odd scalar and the charged scalars $m_A = m_{H^\pm}$ in the type II 2HDM, with the other parameters specified in Eq. (34). The displayed points pass all the theoretical and experimental constraints discussed in section 2.1. The color bar indicates the energy scale $\Lambda_{4\pi}$ at which one of the quartic couplings of the parameter point reaches the naive perturbative bound 4π (for points with $\Lambda_{4\pi} < 10$ TeV). Points with $\Lambda_{4\pi} < m_A$ or m_H are indicated in gray, and points with a short-lived EW vacuum are shown in red. Yellow points feature $\Lambda_{4\pi} \geq 10$ TeV. The black line circumscribes all the points that feature a strong FOEWPT (see text for details).

restrict the analysis to parameter benchmarks for which our perturbative analysis is applicable. Since we are interested in FOEWPTs, we explore a parameter space region where relatively large quartic couplings are present. A key check on the validity of our perturbative calculation of the quantities that characterize the FOEWPT is to make sure that at the energy scales relevant for our analyses the values of the couplings remain in the perturbative range $|\lambda_i| < 4\pi$ (see section 2.3 for details). In Fig. 1 we show the analyzed parameter space in the (m_H, m_A) plane of the 2HDM of type II as specified in Eq. (34). For each point we indicate the energy scale $\Lambda_{4\pi}$ at which one of the 2HDM quartic couplings reaches the naive perturbative bound 4π . The lower-right corner in which no points are shown is excluded from the requirement on the tree-level potential to be bounded from below, imposed via **ScannerS**.¹¹ In the lower right strip we find points with $\Lambda_{4\pi} \geq 10$ TeV, which are indicated in yellow. On the other hand, we find that a large part of the parameter space that is allowed by the constraints discussed in section 2.1 features relatively low

¹¹Such parameter points could still feature a bounded potential upon inclusion of loop corrections [111]. We did not include this possibility in our analysis because we focus here on the thermal evolution of the potential. Including the boundedness check for the loop-corrected scalar potential at zero temperature is computationally much more expensive compared to the application of the tree-level conditions which were determined in compact analytical form [112].

values for $\Lambda_{4\pi}$, smaller than 10 TeV. This feature arises as a consequence of the sizeable values of the quartic couplings λ_i at the initial scale $\mu_0 = v$ that are required to achieve large splittings among the scalar masses, as described in section 4. In particular, our scan contains points for which $\Lambda_{4\pi} < m_A = m_{H^\pm}$ or $\Lambda_{4\pi} < m_H$, which are shown in gray in Fig. 1. Since for these points the perturbativity bound is reached for an energy scale that is lower than one of the involved masses, we regard such a situation as unphysical. Accordingly, we consider this parameter region as excluded and will not analyze it further. As will be discussed below, this region exclusively features scenarios where the global minimum of the potential at $T = 0$ is the origin of field space. Consequently, this additional constraint does not exclude parameter points that otherwise would predict a FOEWPT. Furthermore, we verified that a subset of points with $\Lambda_{4\pi} < m_A = m_{H^\pm}$ or $\Lambda_{4\pi} < m_H$ features a short-lived EW minimum, i.e. the probability for quantum tunnelling from the EW minimum into the deeper minimum (the origin of field space) in this case is such that it gives rise to a lifetime of the EW vacuum that is substantially smaller than the age of the universe.¹² The points with a short-lived EW vacuum are shown in red in Fig. 1. Finally, all the points that feature a strong FOEWPT in Fig. 1 are circumscribed by a solid black line. The strong FOEWPT region is characterised by

$$\xi_n = \frac{v_n}{T_n} > 1, \quad (35)$$

where v_n is the vev in the minimum adopted by the Universe at the nucleation temperature T_n . We stress that for values of ξ_n substantially smaller than 1 it becomes numerically impossible to distinguish between a first- and a second-order phase transition in a perturbative analysis, and such a distinction would then require to take into account non-perturbative effects [8, 113].

We now discuss the different kinds of symmetry-breaking patterns that occur in the analyzed parameter space. In the upper plot of Fig. 2, we indicate six qualitatively distinct zones of the (m_H, m_A) plane of the 2HDM of type II shown in Fig. 1, labelled by A, B, C, D, E and F (as discussed above, in our analysis we regard the gray/red points as excluded). Each of the six zones features a different temperature evolution of the vacuum configuration of the 2HDM Higgs potential. The red line divides the mass plane into two regions. The points above and to the left of the red line feature at $T = 0$ a global minimum at the origin of field space, whereas those below and to the right of the red line have the EW minimum as global minimum at $T = 0$. The different zones in the upper plot of Fig. 2 are analyzed individually in the six plots shown in the lower part. These plots indicate the typical temperature dependence of the minima of the potential for each of the six labelled regions (where the specific point is taken where the label is located). The six benchmark points have been analyzed with `cosmoTransitions` up to a temperature $T_{\max} = 550$ GeV. The blue lines indicate the temperature evolution of $v_{\min} \equiv \sqrt{v_1^2 + v_2^2}|_{\min}$ evaluated at the minimum where the electroweak symmetry is broken. The absence of a blue line for a given temperature indicates that no EW symmetry breaking minimum exists at this temperature. The orange line shows the temperature dependence of the minimum located at the origin of field space. The absence of this line for a given temperature shows that there is no (local or global) minimum at the origin of field space. The vertical dashed red lines show the temperature at which the two minima involved in the transition are degenerate, i.e. the critical temperature. The label ‘‘origin’’

¹²The calculation of the lifetime of the EW vacuum relies on the computation of the four-dimensional euclidean bounce action instead of the three-dimensional bounce action that determines the decay rate of the false vacuum at finite temperature. It should also be noted that in the scenario investigated here the presence of the global minimum in the origin only arises at the loop level, such that a tree-level analysis of the EW vacuum stability would not be sufficient here.

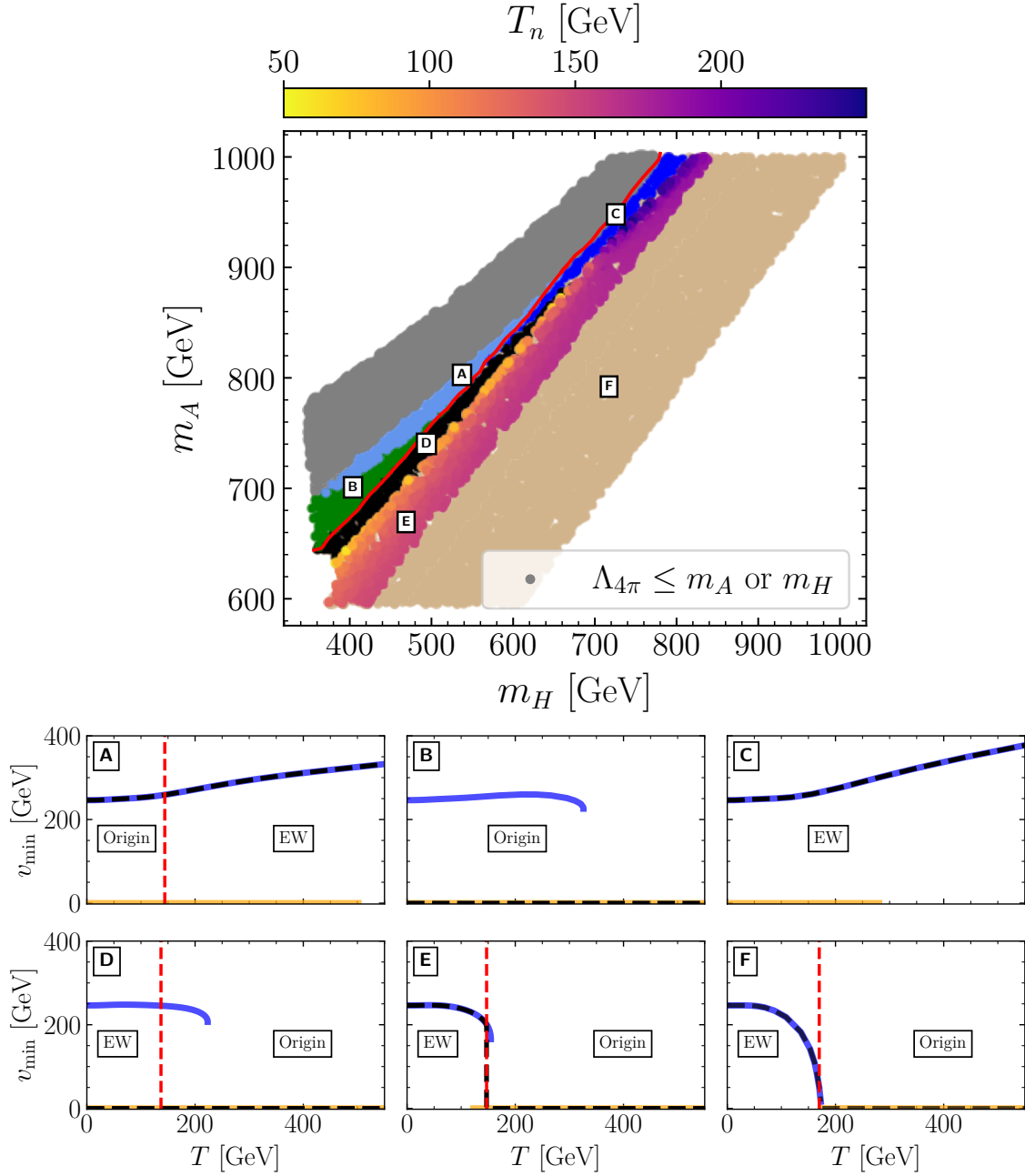


Figure 2: Top: The parameter plane as shown in Fig. 1, with zones featuring qualitatively different thermal histories of their vacuum structure labelled as A, B, C, D, E and F. The red line separates the region with a zero-temperature global minimum at the origin of field space (left) from the region with a zero-temperature electroweak global minimum (right). Bottom: characteristic temperature dependence of v_{\min} for the local minima of the potential for each of the six labelled regions. The blue lines indicate the temperature evolution of v_{\min} evaluated at the minimum where the electroweak symmetry is broken. The orange lines denote how the minimum where the electroweak symmetry is unbroken evolves. The dashed black lines show the vacuum configuration adopted by the universe taking into account phase transitions between co-existing minima. The vertical red lines show the critical temperature, and the labels “origin” and “EW” indicate the global minimum of the potential.

corresponds to a range of temperatures where the origin is the global minimum of the potential, and “EW” indicates a global minimum where the EW symmetry is broken. Taking into account the possible transitions between coexisting minima, the dashed black line indicates the temperature dependence of the vev actually adopted by the universe for each of the benchmark scenarios.

The parameter points with a zero-temperature global minimum at the origin, i.e. the points on the upper left of the red line, are classified into two different zones (A and B). We find that a zero-temperature vacuum stability analysis would allow those points as they all feature meta-stable EW minima whose lifetime is compatible with the age of the universe. The benchmark point belonging to zone A has an EW-broken minimum for the entire temperature range explored, whereas a minimum at the origin only appears for temperatures below $T \sim 500$ GeV. Consequently, the adopted vacuum configuration at high temperature is the one breaking the EW symmetry, and zone A features EW SnR at high temperature. This implies that the breaking of the EW symmetry in the early Universe would have taken place at temperatures substantially above the EW scale (in particular $T > T_{\max}$). Such a high value of the transition temperature can have profound consequences in the context of EW baryogenesis and the related phenomenology at colliders or other low-energy experiments searching for CP-violating effects. In view of those features and of the existing limits on BSM physics around the EW scale at the LHC, the proposal of EW *high-scale* baryogenesis has gained attention in recent years [25, 63, 91–94, 114–116]. Based on the perturbative treatment of the effective potential, we find in this work that the 2HDM, or more broadly speaking extensions of the SM containing a second Higgs doublet, could feature EW SnR and possibly allow for EW baryogenesis at energy scales much higher than the EW scale. On the other hand, for the benchmark scenario belonging to zone B, the only existing minimum at T_{\max} is the minimum at the origin, i.e. the EW symmetry is restored at the maximum temperature that we have analyzed. The broken phase appears for temperatures below $T \sim 325$ GeV, but never becomes deeper than the minimum at the origin, which remains the global minimum for all T . A phase transition into the broken phase is not possible, and the EW symmetry is preserved as the temperature approaches zero. Consequently, this parameter region is regarded as unphysical and therefore excluded.

Now we turn to the analysis of the parameter space region that features a global EW minimum at $T = 0$, located on the lower right side of the red line in the upper plot of Fig. 2. Here we identify four qualitatively different zones depending on their thermal histories (C, D, E, F). For the benchmark point of region C, an EW symmetry breaking minimum exists already at T_{\max} , whereas no minimum of the potential at the origin exists at this temperature. Consequently, this zone exhibits EW SnR at high temperature. The EW minimum is always deeper than the one at the origin, which for our chosen benchmark within this region appears for temperatures below $T \sim 280$ GeV, such that no transition to the minimum at the origin can occur, and the parameter points in this region are, at least in principle, not excluded (in order to definitely determine whether such points are physically viable, one would require a detailed analysis of the behaviour of the scalar potential at even higher temperatures).

Region D features the phenomenon of vacuum trapping. In the benchmark scenario shown in plot D, the EW symmetry is restored at high temperature, and the EW phase appears for temperatures below $T \sim 225$ GeV. Even though a critical temperature exists in this scenario, the condition Eq. (18) is never satisfied, and as a consequence the universe remains trapped in a false vacuum at the origin as $T \rightarrow 0$. This parameter region is therefore not phenomenologically viable and has to be excluded. The possibility of vacuum trapping in the thermal history of the universe and its phenomenological implications will be further discussed in section 4.2.

All the points in region E feature a strong FOEWPT, where the quantity ξ_n meets the condition (35). The plot E exemplifies the typical temperature dependence of the vacuum configuration for one of such parameter points. In this benchmark scenario, the EW symmetry is restored at T_{\max} . The EW minimum appears for temperatures below $T \sim 155$ GeV, and a strong FOEWPT takes place at a nucleation temperature $T_n \approx 140$ GeV. The nucleation temperatures for all points in zone E are given by the color coding in the upper plot of Fig. 2. In region E gravitational wave signals that are sufficiently strong to be detected by LISA could potentially be generated. In section 4.2.2, we will discuss zone E regarding the possible detectability of such GW signals by LISA.

Finally, the points in zone F feature either a weak FOEWPT with $\xi_n < 1$ or a second-order EW phase transition.¹³ The plot F shows a specific benchmark in this region with a second-order phase transition (or a very weak FOEWPT) taking place at $T \sim 170$ GeV. At low temperature the minimum adopted by the universe breaks the EW symmetry, whereas the minimum adopted at high temperature is located at the origin of field space and therefore the EW symmetry is restored.

To summarize the above discussion, taking into account the requirement that the universe has to reach the correct minimum that breaks the EW symmetry at zero temperature has shown that the regions B and D are unphysical and have to be excluded.

4.2 Phenomenological consequences of vacuum trapping

Vacuum trapping, as outlined in section 3.3, corresponds to the situation where the universe remains trapped in an EW symmetric phase while it cools down, even though a deeper EW symmetry breaking minimum of the potential exists at zero temperature. The potential in this case is such that Eq. (18) is never fulfilled at any temperature at which the EW symmetry breaking minimum is deeper than the minimum at the origin.¹⁴ Several recent analyses [24, 25, 32] have noted the importance of this phenomenon for the phenomenology of models with extended Higgs sectors, in particular regarding the possibility of a FOEWPT, the realization of EW baryogenesis, or the production of a stochastic GW background. As we will show in the following, taking into account the constraints from vacuum trapping has an important impact on the prospects for probing parameter regions featuring such phenomena at particle colliders. We start with an analysis of the implications of vacuum trapping for parameter regions in which EW baryogenesis could occur. Afterwards we discuss the impact of vacuum trapping on the possibility of generating GW spectra during a FOEWPT in the 2HDM with a sufficient amplitude to be detectable at future GW observatories.

4.2.1 Implications for electroweak baryogenesis

Although the LHC has set important limits on the presence of additional Higgs bosons at the EW scale, the 2HDM remains compatible with those limits as a viable framework for the explanation of the matter–antimatter asymmetry of the Universe by means of EW baryogenesis [15]. In addition to new sources of CP-violation that can be present in the 2HDM compared to the SM, another vital

¹³The numerical precision of the calculation of ξ_n is not sufficient to distinguish between a very weak FOEWPT, $\xi_n \ll 1$, and a second-order EW phase transition, but for the purpose of our paper such a distinction is of no phenomenological relevance anyway.

¹⁴We stress that in the 2HDM analysis presented in this paper we did not encounter vacuum trapping in any false minimum other than the one located at the origin.

ingredient for the realization of baryogenesis is the presence of a strong FOEWPT. In the following, we will focus on the criterion of a FOEWPT.¹⁵ As an indicator of the presence of a FOEWPT that is sufficiently strong for allowing the generation of the observed matter–antimatter asymmetry, the criterion

$$\xi_c = \frac{v_c}{T_c} > 1, \quad (36)$$

has often been used in the 2HDM and extensions thereof [28–31, 117–124]. Here v_c is the vev in the EW symmetry breaking minimum at the critical temperature T_c , and ξ_c is denoted as the *strength* of the transition. This so-called baryon number preservation criterion [56] (see also Ref. [53] and references therein) yields a condition for avoiding the wash-out of the baryon asymmetry after the EW phase transition. However, in parts of the literature it is also used as a sufficient requirement for the presence of a FOEWPT via the existence of the critical temperature T_c at which the EW minimum becomes the global minimum. In contrast to this, we will show in this section that the criterion of Eq. (36) is not a reliable indicator of the occurrence of a FOEWPT in the 2HDM (see also Ref. [56]). As analyzed below, the calculation of the nucleation (or transition) temperature with the help of Eq. (18) is crucial, not only in order to assess the actual strength of the FOEWPT which happens at temperatures $T_* \sim T_n < T_c$, but more importantly to determine whether the FOEWPT takes place at all. The nucleation criterion shown in Eq. (18) should then be used in order to accurately determine the 2HDM parameter space that reaches the EW vacuum configuration at zero temperature as a result of a FOEWPT, whereas a criterion just based on the existence of T_c would include also parameter space regions that are unphysical due to the occurrence of vacuum trapping.

In Fig. 3 we show the parameter scan points in the (m_H, m_A) plane, where the color coding indicates (for both plots) the values of ξ_c for parameter points for which $\xi_c > 1$. According to several existing analyses (see the discussion above) these points would be classified as featuring a strong FOEWPT that could generate the observed baryon asymmetry of the Universe. The dark gray points in Fig. 3 correspond to the region with a zero-temperature global minimum at the origin of field space (corresponding in Fig. 2 to the combined area of the gray points and of the zones A and B). These points are thus not relevant for the present analysis (being either unphysical or featuring EW SnR up to the highest temperatures analyzed in our scan). The light gray region depicts parameter points that, while featuring a zero-temperature global EW minimum, do not meet the condition imposed on the strength of the transition based on T_c , see Eq. (36). The dashed black line circumscribes the points that meet the more appropriate requirement for a strongly FOEWPT based on T_n , defined in Eq. (35) (coinciding with the solid black line in Fig. 1 and the zone E in Fig. 2). The left plot of Fig. 3 shows that the region with the highest values of ξ_c (corresponding to the pink points) lies at the border with the dark gray region, and features transition strength values up to $\xi_c \sim 6$, which would be particularly well suited for EW baryogenesis. However, taking into account the constraint from vacuum trapping (zone D in Fig. 2), indicated by the black points in the right plot of Fig. 3, which are painted above the points displaying the value of ξ_c , one can see that the parameter region featuring the highest ξ_c values is in fact excluded as a consequence of vacuum trapping. After taking into account this constraint, the maximum allowed value for ξ_c is $\xi_c \sim 1.8$ (instead of $\xi_c \sim 6$), indicated by a vertical black line inside the color bar on the right plot of Fig. 3. At the same time, Fig. 3 highlights that vacuum trapping not only has a strong impact on the maximum values of ξ_c that can be achieved in the physically viable parameter regions, but it is also crucial for determining the 2HDM parameter

¹⁵We assume that the required sources of CP violation do not have an impact on the dynamics of the phase transition and can therefore be neglected in our analysis.

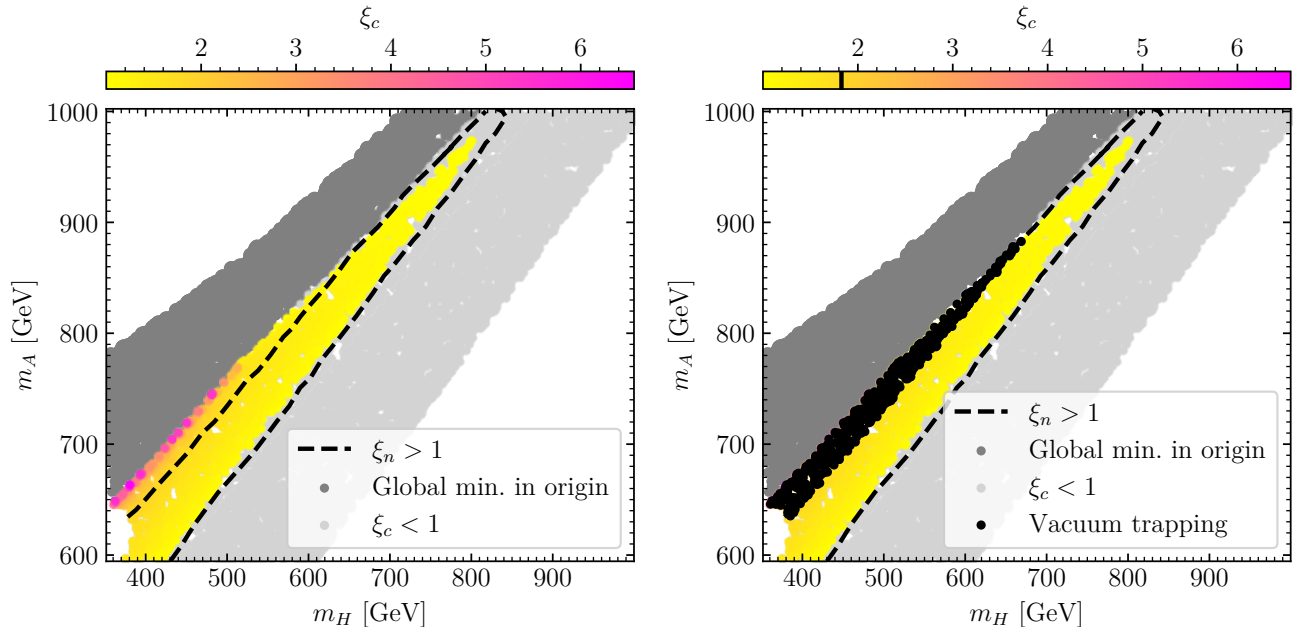


Figure 3: The parameter plane as shown in Fig. 1, where for both plots the points shown in light gray feature a second-order EW phase transition or a FOEWPT with $\xi_c < 1$, whereas for the dark gray points the global minimum is in the origin (corresponding to the area of the gray points and the zones A and B in Fig. 2), and accordingly the points do not feature an EW phase transition within the investigated temperature range. The colored points feature a critical temperature T_c at which the EW minimum becomes the global one, where the color coding of the points indicates the value of ξ_c . The dashed black line circumscribes all points that feature a FOEWPT with $\xi_n > 1$. In addition to what is shown in the left plot, the black points in the right plot (which are painted above the points displaying the value of ξ_c) indicate the parameter region that is excluded as a consequence of vacuum trapping, and the vertical black line in the color bar indicates the maximum value of ξ_c that is found after the incorporation of the constraint from vacuum trapping.

region that features a FOEWPT: the constraint from vacuum trapping excludes the parameter region in the left plot of Fig. 3 with the largest values for the mass splitting $m_A - m_H$ for a fixed value of m_H . This has important consequences for the prospects of probing 2HDM scenarios featuring a strong FOEWPT at current and future colliders. For instance, the cross section for the LHC signature $pp \rightarrow A \rightarrow ZH$ (which would be a “smoking gun” signature for the existence of such a strong FOEWPT in the 2HDM [15, 28, 30]) depends on the mass splitting between A and H , since the branching ratio for the decay $A \rightarrow ZH$ grows with increasing mass splitting. The constraint from vacuum trapping can then place an upper limit on the cross section for such an $A \rightarrow ZH$ signature within the 2HDM (see e.g. [32]). A more detailed discussion on the collider phenomenology of the parameter region with a FOEWPT will be given in section 4.3.

Finally, we point out that the black-dashed line in Fig. 3, defined by the criterion $\xi_n > 1$, circumscribes also light-gray points at the upper end of the m_A, m_H mass ranges considered here. Thus, in this mass region we find parameter points that feature strongly FOEWPTs based on the transition strength evaluated at T_n , but would not satisfy the corresponding criterion for avoiding the wash-out of the baryon asymmetry evaluated at T_c . As a consequence, the criterion based on T_n allows for larger values of m_A and m_H compared to the (potentially misleading) criterion based on T_c .

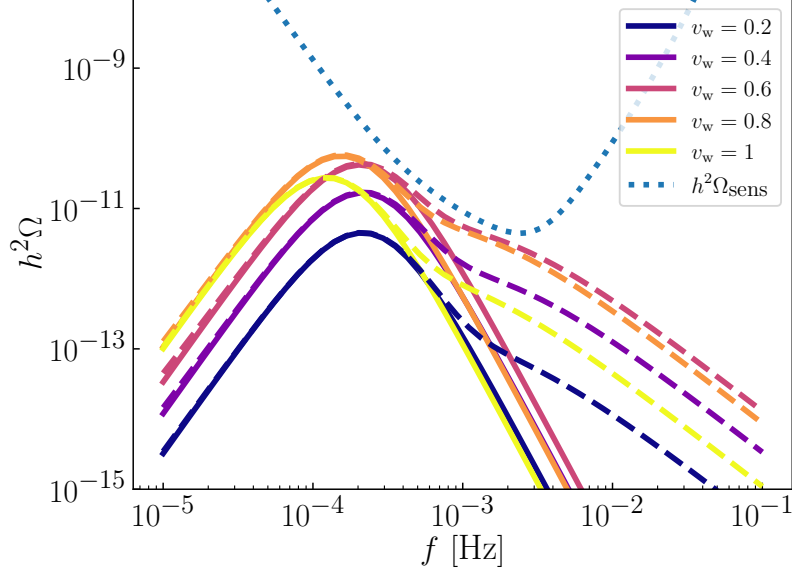


Figure 4: GW spectrum for a 2HDM benchmark point with BSM scalar masses $m_H = 419.33$ GeV and $m_A = m_{H^\pm} = 663.05$ GeV, yielding a FOEWPT with $T_n = 52.43$ GeV, $\alpha = 0.172$ and $\beta/H = 26.2$. $h^2\Omega_{\text{GW}}$ predictions for different bubble wall velocity values ($v_w = 0.2, 0.4, 0.6, 0.8, 1$) are shown in different colors for the concave curves. The dashed lines show the predictions where the turbulence contribution to $h^2\Omega_{\text{GW}}$ is included, while this contribution is omitted for the solid lines. The dotted curve indicates the nominal sensitivity of LISA to stochastic sources, $h^2\Omega_{\text{sens}}$.

4.2.2 Gravitational waves

As discussed in section 3.5, a cosmological FOEWPT can produce a stochastic GW background that could be observable by the future LISA GW interferometer. We now analyze the production of GWs from a FOEWPT in the 2HDM, discussing the quantities T_* , α , β/H and v_w and studying the prospects for the detection of the GW signals at LISA. We will specifically show that the phenomenon of vacuum trapping puts severe limitations on the GW SNR achievable at LISA in the 2HDM.

We first briefly discuss the dependence on the bubble wall velocity v_w . In Fig. 4 we show, for different values of v_w , the predictions for the GW spectrum of a specific 2HDM benchmark point yielding a potentially large GW signal with BSM scalar masses $m_H = 419.33$ GeV and $m_A = m_{H^\pm} = 663.05$ GeV, yielding a FOEWPT at a temperature of $T_n = 52.43$ GeV with $\alpha = 0.172$ and $\beta/H = 26.2$. The solid lines correspond to the predictions for $h^2\Omega_{\text{GW}}$ omitting the contribution from turbulence in the plasma, whereas for the dashed lines this contribution is included. Fig. 4 also shows the LISA nominal sensitivity obtained from its noise curve (see section 3.5 for details). The bubble wall velocity has a strong impact on the GW spectrum, shifting the position of the peak of the GW signal and significantly modifying its amplitude. These effects translate into a large variation of the SNR at LISA (assuming a duration of the LISA mission of $\mathcal{T} = 7$ years) for different values of v_w , as shown in Table 1. The highest SNR occurs for $v_w \sim 0.6$ and for GW signals in which the turbulent motion of the primordial plasma was considered as a source of GWs. The feature that the highest SNR occurs for about this value of v_w is fairly generic in the 2HDM (i.e. it is not specific for the benchmark chosen for illustration). We thus consider the contribution from turbulence to $h^2\Omega_{\text{GW}}$ and use $v_w = 0.6$ for the predictions

v_w	turb.	no turb.
0.2	23	18
0.4	149	67
0.6	522	153
0.8	431	101
1	70	28

Table 1: LISA SNR of the GWs for the 2HDM benchmark scenario shown in Fig. 4 for different values of the bubble wall velocity v_w , taking into account the effect of turbulence as a source of GWs ("turb.") and omitting it ("no turb.").

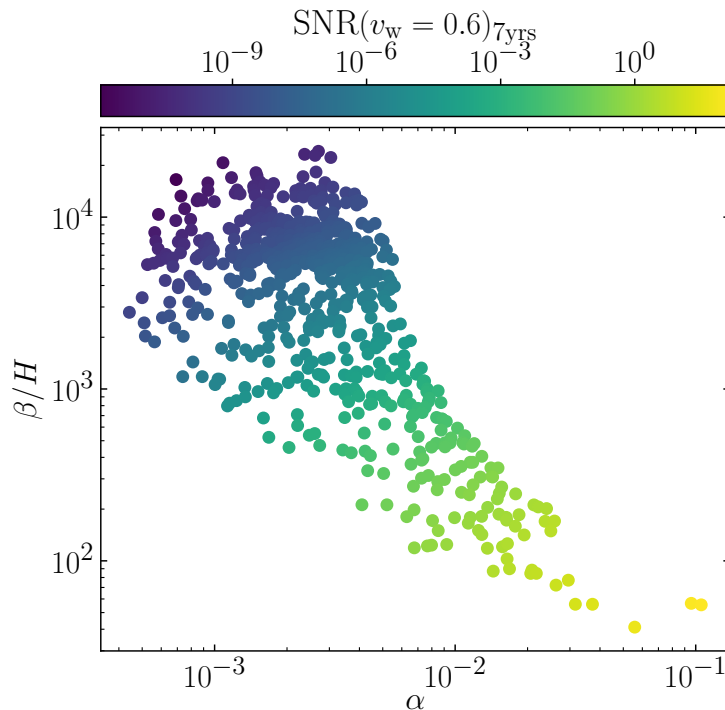


Figure 5: Parameter points of the scan shown in Fig. 1 in the $(\alpha, \beta/H)$ plane, with the color-code indicating the SNR at LISA (assuming $v_w = 0.6$ and $\mathcal{T} = 7$ years).

of the GW signals in the rest of this work in order to investigate the maximum sensitivity to these signals.

In Fig. 5 we show the values of the inverse duration of the phase transition β/H in dependence of the strength α for all the points in our random scan satisfying $\xi_n > 1$ (region E in Fig. 2). The color code indicates the value of the SNR at LISA (for $v_w = 0.6$ and a LISA mission duration $\mathcal{T} = 7$ years). As expected, the points with the largest values of α and the smallest values of β/H feature the largest SNRs for LISA. The SNR values range over several orders of magnitude for relatively small changes in the values of the masses m_H and m_A , as will be shown below. This is a consequence of the strong sensitivity of the predicted GW spectra to the underlying 2HDM model parameters (specifically, the BSM scalar masses).¹⁶ We also note that within the parameter space displayed in Fig. 3 the strongest GW signals are concentrated in a very narrow region of the $(m_H,$

¹⁶Such a strong sensitivity has already been observed in Ref. [15] (see, for instance, Fig. 3 therein). Similar observations have been made in the triplet extension of the SM [125].

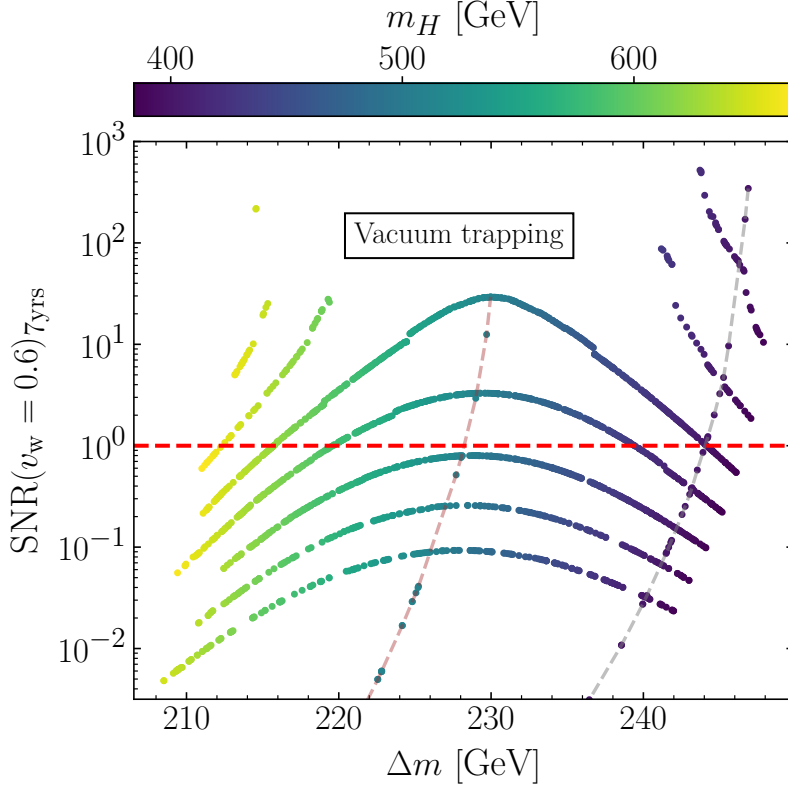


Figure 6: SNR at LISA (for $v_w = 0.6$ and $\mathcal{T} = 7$ years) against $\Delta m = m_A - m_H$ for the parameter points of the dedicated finer scan (see text) with $m_A = a m_H + b$, $a = 0.87$ and $b = \{291, 292, 293, 294, 295, 296, 297\}$ GeV. The color coding of the points indicates the values of m_H .

m_A) mass plane adjacent to the parameter space featuring vacuum trapping, and thus only a very small fraction of the 2HDM neutral BSM mass plane could be probed by LISA.

In order to explore in detail the region of parameter space where the strongest GW signals are present, we have performed a linear regression of the points featuring $\text{SNR} \gtrsim 0.5$, which are effectively found along a line given by $m_A = a m_H + b$, with $a = 0.87$ and $b = 295$ GeV. We have then performed a finer scan of the regions adjacent to this line along parallel lines in the m_H - m_A plane by shifting the value of b in steps of 1 GeV, i.e. for $b \in \{291, 292, 293, 294, 295, 296, 297\}$ GeV. The results of this dedicated finer scan can be seen in Fig. 6, where we show the GW SNR at LISA in dependence of the mass difference $\Delta m \equiv m_A - m_H$ (we recall that we set $m_A = m_{H^\pm}$ and $M = m_H$ throughout this work). The color code indicates the value of m_H . Bearing in mind the large uncertainties of the predictions for the GW signal from a FOEWPT, as discussed in section 3.5, we consider as potentially detectable by LISA any SNR of $\mathcal{O}(1)$, and mark the corresponding (indicative) threshold $\text{SNR} = 1$ in Fig. 6 as a horizontal dashed red line. The largest SNR values that we find in our finer scan are $\mathcal{O}(100)$ to $\mathcal{O}(1000)$ (such points could therefore be detected by LISA for $\mathcal{T} < 7$ years and/or with a substantially different assumption on v_w). For $b = 296, 297$ GeV, Fig. 6 shows a region ranging from $\Delta m \sim 215$ GeV to $\Delta m \sim 240$ GeV where the parameter points yielding the largest SNR values are found to be unphysical as a consequence of vacuum trapping (the corresponding lines of benchmark points in Fig. 6 are thus interrupted in this region). Large values of the SNR of $\mathcal{O}(100 \text{ GeV})$ or above are only found at the lower and the upper end of the Δm scan range, where the occurrence of vacuum trapping is just barely avoided. In fact, a further scanned line of parameter points in Fig. 6 with $b = 298$ GeV is entirely excluded as a

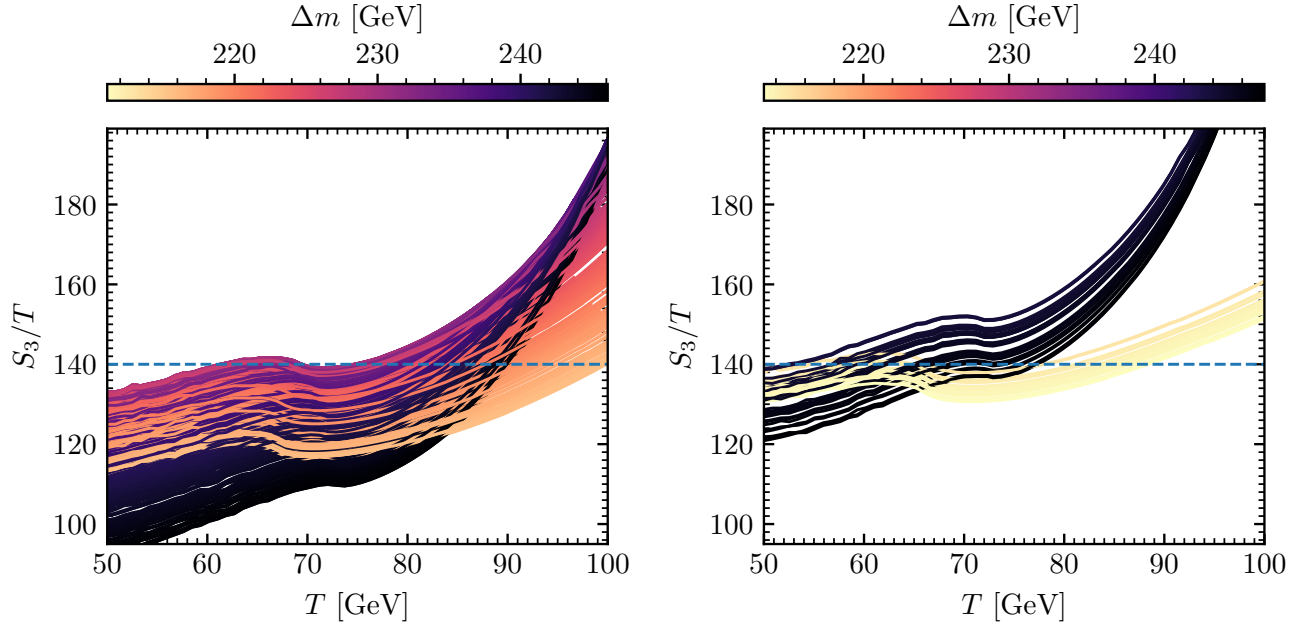


Figure 7: $S_3(T)/T$ as a function of T with the color coding indicating the value of $\Delta m = m_A - m_H$. In the left plot we show the results for scan points corresponding to $b = 295$ GeV in the dedicated scan of Fig. 6, whereas in the right plot we show the results for the $b = 297$ GeV line of points (which is interrupted at intermediate values of Δm due to the presence of vacuum trapping). The dashed blue horizontal line indicates $S_3(T)/T = 140$. The crossing of the lines for $S_3(T)/T$ with the dashed-blue line for decreasing T signals the onset of the phase transition at the respective temperature (see the nucleation criterion in Eq. (18)).

result of vacuum trapping.

In addition to the finer scan discussed above, we show in Fig. 6 the SNR resulting from scans with fixed value of m_H and increasing Δm , specifically for $m_H = 400$ GeV (gray dashed line in Fig. 6) and $m_H = 511$ GeV (brown dashed line in Fig. 6). These additional lines make even more visible the drastic change of the SNR at LISA as a consequence of a variation of the masses $m_A = m_{H\pm}$ by only a few GeV. Moreover, both lines show the same features regarding vacuum trapping as discussed above. This whole analysis demonstrates that the phenomenon of vacuum trapping severely limits the possibility of achieving large values of the SNR at LISA from GW production in the 2HDM.

The strong dependence of the SNR on the 2HDM model parameters, pointed out at the beginning of this section and shown explicitly in Fig. 6, is related to the fact that the largest GW signals occur just at the border of the parameter space region in which the Universe remains trapped in the false vacuum. In order to investigate this in more detail, we depict in Fig. 7 the values of the bounce action over the temperature, $S_3(T)/T$, for temperatures lower than T_c , such that a FOEWPT can occur. In the left panel of Fig. 7 we show $S_3(T)/T$ for $b = 295$ GeV in our detailed scan from Fig. 6 (corresponding to the benchmark line in Fig. 6 with the largest values of the SNR without featuring a gap as a consequence of vacuum trapping): bearing in mind that we assume that the onset of the FOEWPT occurs for $S_3(T)/T \sim 140$ (recall the discussion in section 3.2), we see that the benchmark lines in the left plot of Fig. 7 with $\Delta m \sim 230$ GeV barely reach $S_3(T)/T \sim 140$, and are thus on the verge of being vacuum-trapped. In the right panel of Fig. 7 we show the corresponding values of $S_3(T)/T$ for the $b = 297$ GeV benchmark set, which features

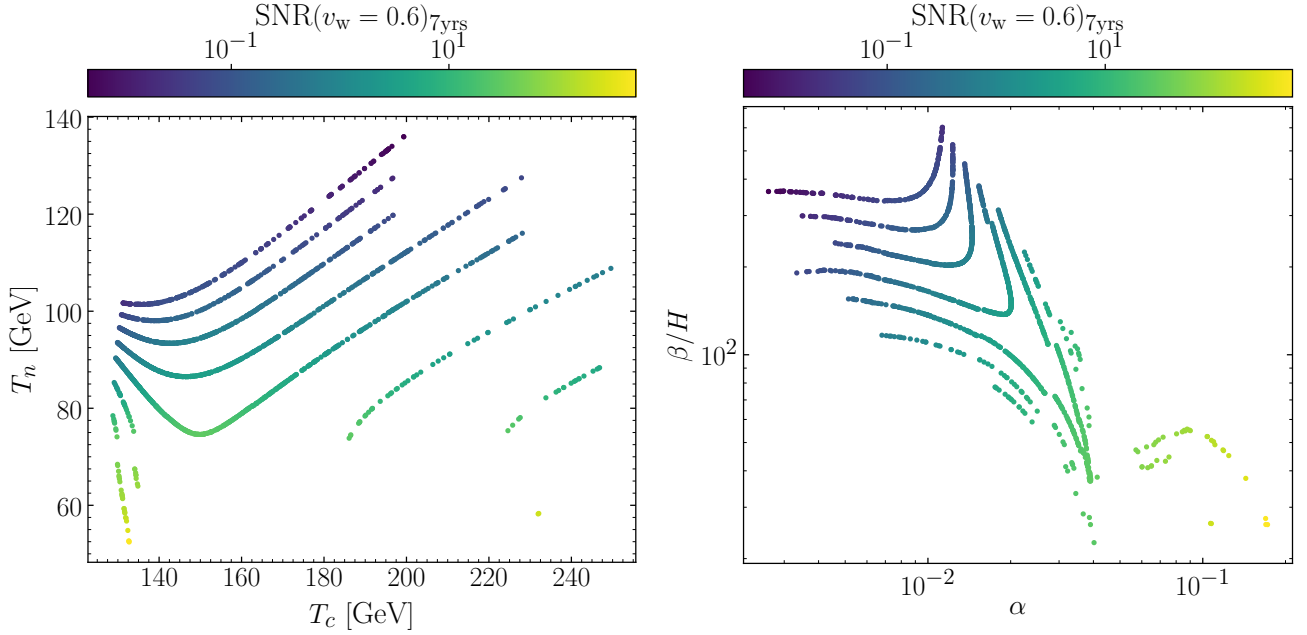


Figure 8: Parameter points of the dedicated finer scan of Fig. 6, in the (T_c, T_n) plane (left panel) and in the $(\alpha, \beta/H)$ plane (right panel), with the color coding of the points indicating the SNR at LISA.

vacuum trapping for Δm in the approximate range $[215, 240]$ GeV (as seen in Fig. 6). As a result, the lines in the right plot of Fig. 7 are separated into two different bundles. For the parameter lines in between these two bundles the prediction remains above $S_3(T)/T = 140$ (depicted as a dashed blue line) over the whole temperature interval $0 < T < T_c$, reflecting vacuum trapping (and those lines are therefore not depicted). In addition, many $S_3(T)/T$ lines have their minima just below the dashed blue line. Since they are on the verge of vacuum-trapping, these lines become rather flat as they approach $S_3(T)/T = 140$, leading to a large variation of T_n (i.e. the temperature at which $S_3(T)/T \simeq 140$ is achieved) within a very small Δm range. As an example, for the black bundle of lines in the right plot of Fig. 7 we have $243 \text{ GeV} < \Delta m < 247 \text{ GeV}$, i.e. a variation within just 4 GeV, while T_n varies in the range $52 \text{ GeV} < T_n < 77 \text{ GeV}$. At the same time, by comparing the two panels of Fig. 7 we observe that a very small change in b from our detailed scan leads to large variations of the T_n behaviour as a function of Δm . The very strong dependence¹⁷ of T_n on subtle changes of the 2HDM masses then feeds into the GW spectra (e.g. $\alpha \sim 1/T_n^4$) and ultimately into the SNRs at LISA. As a result, values of the SNR > 1 are found only in a very restricted region of the 2HDM parameter space, in the vicinity of the vacuum-trapping (unphysical) parameter region.

In Fig. 8 we explicitly show, for the detailed scan introduced in Fig. 6, the dependence of

¹⁷We stress that the FOEWPT nucleation criterion used here, $S_3(T)/T = 140$, is only an approximation [20], and also the computation of the tunneling rate given by Eq. (15) suffers from sizable theoretical uncertainties from missing higher-order contributions (both in the prefactor $A(T)$ and in the perturbative formulation of V_{eff} , affecting S_3) as well as from the issues of gauge dependence [56] and renormalization scale dependence (see App. A). Yet, such uncertainties only have a sizable impact on parameter points close to the vacuum-trapping region, whereas regions leading to weaker GW signals (i.e. regions that are not in the vicinity of the vacuum-trapping region) do not feature such large uncertainties in the SNR prediction. Thus, our conclusion that within the parameter region featuring a FOEWPT the points giving rise to a GW signal that could potentially be observable at LISA occur only in a small region in the vicinity of the region that is excluded by vacuum trapping is therefore robust even in view of these issues.

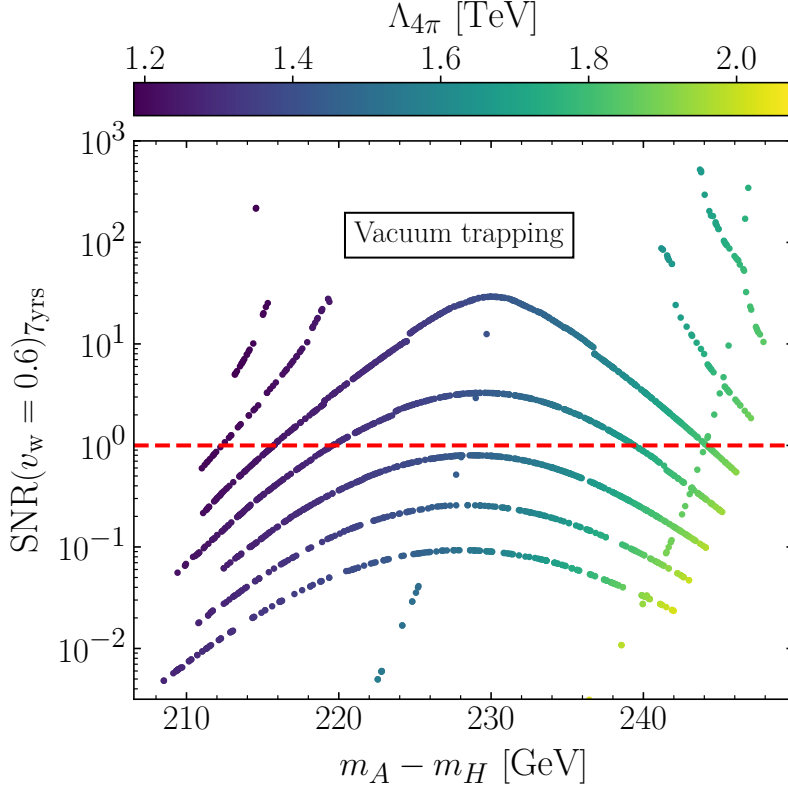


Figure 9: Parameter points of the dedicated finer scan of Fig. 6, in the $(\Delta m = m_A - m_H, \text{SNR})$ plane, with the color coding indicating the energy scale $\Lambda_{4\pi}$ at which one of the quartic couplings reaches the naive perturbative bound 4π .

the LISA SNR on the quantities T_n , α and β/H . In the left plot of Fig. 8 we show the relation between the nucleation temperature T_n and the critical temperature T_c for this scan (with color-code indicating the SNR at LISA). The large difference between the two temperatures for all the points in this scan reaffirms the necessity of computing the nucleation temperature in order to make reliable predictions concerning the FOEWPT properties in the 2HDM, since not even a qualitative description of the strength of the phase transition is possible based on the knowledge of the critical temperature. In the right panel of Fig. 8 we show the corresponding detailed scan points in the $(\alpha, \beta/H)$ plane, from which an intricate dependence of both parameters on the 2HDM masses can be inferred by correlating with the information from Fig. 6. Compared to the broader scan shown in Fig. 5, we find here a substantially smaller range of β/H (down to $\beta/H \sim 23$) and overall larger values of α (up to $\alpha \sim 0.17$). We stress here that values of $\beta/H \ll 100$ are an indicator of a scenario that is close to featuring vacuum trapping (see e.g. the discussion in [77]).

Finally, we emphasize once more that a FOEWPT in the 2HDM requires sizable quartic scalar couplings λ_i such that a potential barrier between the two minima involved in the transition can be generated via radiative and/or thermal loop corrections. The RGE evolution of such sizable quartic couplings can drive the theory into a non-perturbative regime already at energies not far from the TeV scale, as discussed in detail in section 2.3 (see also Ref. [126] for a one-loop analysis). This issue is most severe for the strongest phase transitions, such as the ones that produce GW signals with sizable SNR values at LISA. We therefore investigate the energy range in which the theory is well-defined for the type II 2HDM parameter regions that could yield an observable GW signal at LISA. In Fig. 9 we show the 2HDM parameter points of our detailed scan in the

($\Delta m = m_A - m_H$, SNR) plane, as in Fig. 6, but now with the color-coding indicating the energy scale $\Lambda_{4\pi}$ at which one of the quartic scalar couplings λ_i reaches the naive perturbative bound 4π (see section 2.3 for details). The value of $\Lambda_{4\pi}$ signals the energy scale μ at (or below) which new BSM physics should be present in order to avoid a Landau pole and to render the theory well-behaved above that energy scale. We observe that the lowest values of $\Lambda_{4\pi}$ in our detailed scan are $\Lambda_{4\pi} \sim 1.2$ TeV, whereas the largest values are found slightly above $\Lambda_{4\pi} = 2$ TeV. By comparing with Fig. 6 we also observe that the smallest values of $\Lambda_{4\pi}$ correlate with the largest values of m_H in the scan, which can have important phenomenological implications (as we discuss in the next section). Altogether, Fig. 9 shows that parameter regions that feature a potentially detectable (SNR > 1) GW signal at LISA would require new-physics effects (e.g. new strongly coupled states) at energy scales that are well within the reach of the LHC. This finding calls for a thorough assessment of the complementarity between LHC (and future collider) searches and GW probes with LISA in these theories.

4.3 Interplay between the HL-LHC (and beyond) and LISA

As already outlined above, the 2HDM parameter regions featuring a GW signal that could potentially be observable at LISA generally predict signatures of BSM physics within reach of the LHC, both from the presence of the 2HDM scalars themselves and from further new (strongly coupled) states that would in some parts of the parameter space be needed to prevent the appearance of a Landau pole close to the TeV scale. In this section, we focus on the collider signals of the 2HDM scalars in view of the prospects for the interplay between the possible observation of a stochastic GW signal from the 2HDM at LISA and collider probes (at the HL-LHC and a future e^+e^- Linear Collider) of the 2HDM states.

4.3.1 GWs at LISA vs. direct BSM searches at the LHC

Given the projected HL-LHC and LISA timelines, the HL-LHC is expected to scrutinize the 2HDM parameter space of relevance for GW searches before the LISA observatory will start taking data. We show that, within the type II 2HDM, for the case where no direct BSM signatures will be detected at the high-luminosity phase of the LHC the resulting limits would essentially exclude the parameter regions giving rise to a potentially observable GW signal at LISA. Thus, the prospects for observing a GW signal at LISA crucially depend on the outcome of the high-luminosity phase of the LHC.

Among the possible collider signatures of the heavy 2HDM scalars, the most promising ones to probe the 2HDM parameter region featuring a FOEWPT consist of Higgs boson cascade decays, due to the sizable mass splittings between the BSM Higgs bosons. Specifically, the production of the CP-odd Higgs boson A that then decays into a Z boson and the heavy CP-even scalar H is a *smoking-gun* collider signature of FOEWPT scenarios in the 2HDM [28]. This signature has been searched for at the LHC with $\sqrt{s} = 8$ TeV and 13 TeV assuming that A is produced via gluon-fusion or in association with a pair of bottom quarks, and utilizing the leptonic decay modes of the Z -boson. The scalar H was required to decay either to a pair of bottom quarks or to a pair of tau leptons [127–129]. However, as already pointed out in Ref. [25], the combination of the current theoretical and experimental constraints in the type II 2HDM pushes m_H to be above the di-top threshold in almost the entire parameter region featuring a FOEWPT. Then, the branching fractions for $H \rightarrow b\bar{b}$ and $H \rightarrow \tau^+\tau^-$ become very small (except for large values of t_β), and searches via these final states do not yield relevant constraints on FOEWPT scenarios. It is instead much

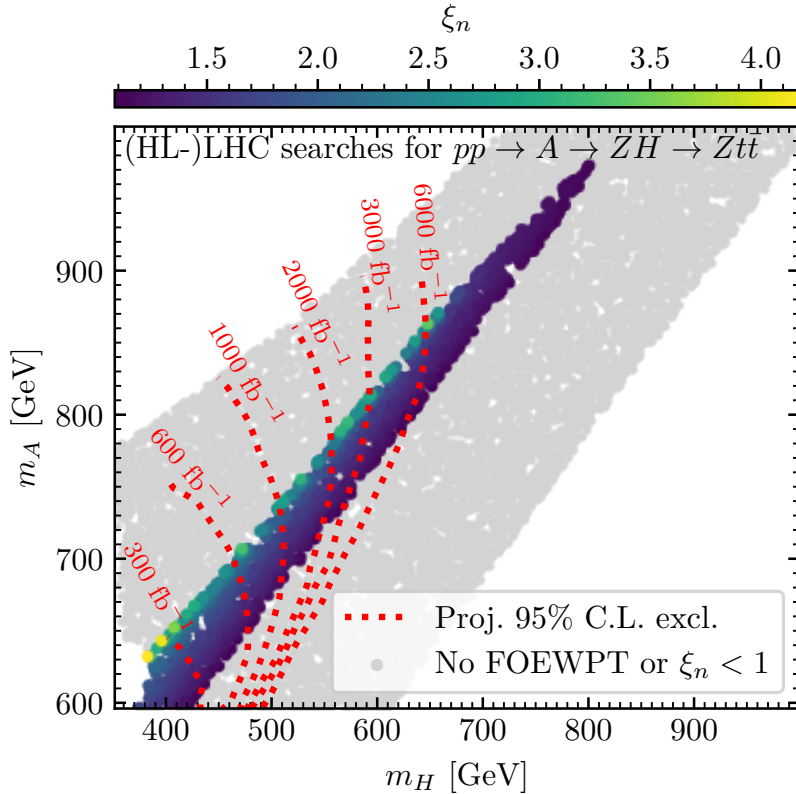


Figure 10: Parameter points of the scan discussed in Sect. 4.1 in the (m_H, m_A) plane, with the color coding indicating the value of ξ_n for the points that feature a strong FOEWPT, i.e. $\xi_n > 1$. The remaining points are shown in gray. The red dashed lines indicate the projected 95% C.L. exclusion regions resulting from the (HL-)LHC searches for the process $pp \rightarrow A \rightarrow ZH$ with H decaying into a pair of top quarks (see text for details).

more promising to search for $A \rightarrow ZH$ signatures with H decaying into a pair of top quarks, and preliminary studies of this final state exist in the literature [130, 131]. Efforts to analyze the $Zt\bar{t}$ final state are ongoing by both the ATLAS [132] and CMS [133, 134] collaborations. We here use the public results on this channel obtained in a Master thesis for the CMS Collaboration (using only the $Z \rightarrow \mu^+\mu^-$ decay mode) for an integrated luminosity of 41 fb^{-1} at 13 TeV [133] to estimate the projected (HL-)LHC sensitivity to the process $A \rightarrow ZH$ in the $Zt\bar{t}$ final state for several integrated luminosities: $\mathcal{L} = 300 \text{ fb}^{-1}$, 600 fb^{-1} , 1000 fb^{-1} , 2000 fb^{-1} , 3000 fb^{-1} and 6000 fb^{-1} (the latter corresponds to the expected combined total integrated luminosity that will be collected by ATLAS and CMS at the HL-LHC). We obtain the predicted 2HDM production cross sections (at NNLO) times branching ratios for the $pp \rightarrow A \rightarrow ZH \rightarrow \mu^+\mu^-t\bar{t}$ signature as a function of m_A and m_H (with the rest of parameters fixed as in Eq. (34)) using SUSHI [51] and N2HDECAY [52]. In Fig. 10 we show the expected 95% C.L. exclusion sensitivity for different values of \mathcal{L} from a naive rescaling of the CMS expected limits by a factor $\sqrt{(41 \text{ fb}^{-1})/\mathcal{L}}$ (which assumes that the present CMS sensitivity is limited by statistics rather than systematics). We emphasize that taking into account also other (leptonic) decay modes of the Z boson yields even stronger projected limits [134]. On the other hand, the preliminary projected cross-section limits do not yet account for all systematic uncertainties, for instance, from the b -tagging efficiencies. The inclusion of such systematic uncertainties could weaken the expected sensitivity. Considering both

aspects, the exclusion regions shown in Fig. 10 can be regarded as fairly conservative estimates. Nevertheless, we verified that even assuming that the cross-section limits are a factor of 2 weaker, the HL-LHC could exclude the parameter region featuring a strong FOEWPT up to masses of $m_H \sim 550$ GeV and $m_A \sim 750$ GeV.

The projected exclusion limits in Fig. 10 are compared with the points of the 2HDM parameter scan discussed in section 4.1, where the parameter points featuring a strong FOEWPT are shown in color (the color-coding indicates the value of ξ_n), and the remaining points are depicted in gray. Already at the end of LHC Run 3 with 300 fb^{-1} (600 fb^{-1} assuming a potential combination of ATLAS and CMS data), a substantial part of the parameter space featuring a strong FOEWPT will be explored, corresponding to values of $m_H \lesssim 470$ GeV (see Fig. 6). In particular, the 2HDM region yielding observable GW signals at LISA with values of $\Lambda_{4\pi} > 2$ TeV (see Fig. 9) will be completely covered by this LHC search during Run 3, and so will be the parameter points with the strongest phase transitions, corresponding to values of $\xi_n \sim 4$. The HL-LHC, with ten times more data, will be able to probe masses up to $m_H \sim 650$ GeV via the $A \rightarrow ZH$ ($H \rightarrow t\bar{t}$) search, covering almost the entire 2HDM region that features a GW signal that could potentially be detectable with LISA (see Fig. 6). This analysis highlights the importance of putting the expectations for GW signals from FOEWPTs that could be detectable by LISA into the context of the projected (HL-)LHC results.

4.3.2 GWs at LISA vs. Higgs boson self-coupling measurements at LHC and ILC

A well-known avenue to probe the thermal history of the EW symmetry, particularly in connection with a possible FOEWPT, is the measurement of the trilinear self-coupling of the Higgs boson at 125 GeV. A FOEWPT is generically associated with a sizable enhancement of the trilinear self-coupling λ_{hhh} as compared to the SM prediction [33, 34].¹⁸ In the following, we determine the values of λ_{hhh} predicted in the 2HDM parameter space regions which feature a FOEWPT, including the regions that would yield a GW signal that could potentially be observable at LISA. According to our treatment of the zero-temperature effective potential from Eq. (4), λ_{hhh} is calculated here at the one-loop level (see Ref. [136] for a discussion of the impact of the dominant two-loop contributions in the 2HDM). In order to align our analysis with the experimental interpretations of bounds on the Higgs boson trilinear self-coupling obtained by the ATLAS and CMS collaborations within the κ -framework, we here define $\kappa_\lambda = \lambda_{hhh}/\lambda_{hhh}^{\text{SM}}$, where $\lambda_{hhh}^{\text{SM}}$ is the tree-level Higgs boson self-coupling prediction of the SM. In Fig. 11 we show the predicted values of κ_λ in dependence of the mass splitting $m_A - m_H$ for the parameter scan from Eq. (34). In the left panel, the various colors indicate the different types of thermal histories (the letter in each region specifies the corresponding thermal evolution of the vacuum according to the description of Fig. 2). As expected, large values of $m_A - m_H$ are correlated with large values of κ_λ . In particular, parameter points featuring a strong FOEWPT (region E) predict values of up to $\kappa_\lambda \sim 2$, and vacuum trapping (region D) excludes part of the parameter space with even larger values of κ_λ . There are still physically viable parameter points predicting values of $\kappa_\lambda > 2$ (regions A and C; we remind the reader that region B is unphysical, see section 4.1), associated with the phenomenon of EW SnR. The plot shows that the largest values of κ_λ occur for 2HDM parameter regions that are not phenomenologically viable (dark-gray points), as these regions feature an energy cutoff $\Lambda_{4\pi}$ that is smaller than the masses of the BSM scalar states, i.e. $\Lambda_{4\pi} < m_A = m_{H^\pm}$ or $\Lambda_{4\pi} < m_H$; a large fraction of these points also features a short-lived EW vacuum (see Fig. 1).

¹⁸This is especially the case for FOEWPTs which are not *singlet-driven* (caused by a singlet scalar field coupling to the SM-like Higgs doublet). For a singlet-driven FOEWPT, it is possible to avoid such large enhancements [135].

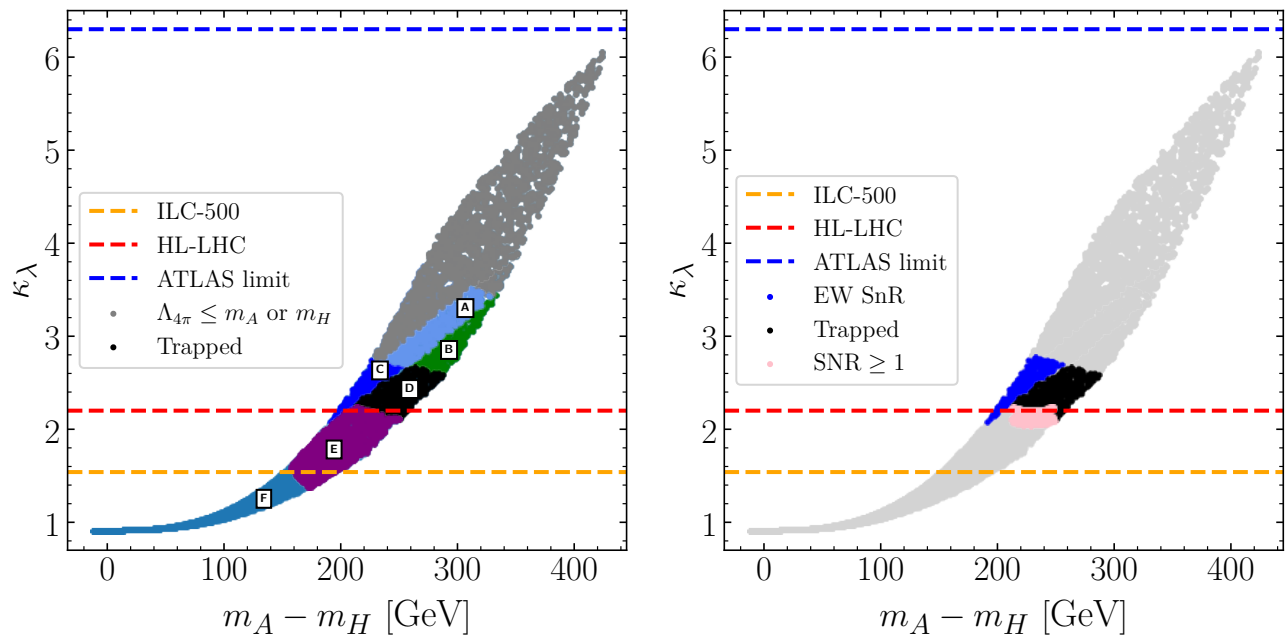


Figure 11: Parameter points from the scan as defined in Eq. (34) with the mass difference $m_A - m_H$ on the horizontal axis and κ_λ on the vertical axis. In the left panel, the color of the points indicates the different kinds of thermal histories: the letter specifies each region according to Fig. 2, and dark-gray points feature $\Lambda_{4\pi} \leq m_A$ or m_H , and/or a short-lived EW vacuum. In the right panel, blue points feature EW SnR, black points feature vacuum trapping (and are therefore unphysical), and pink points predict a FOEWPT with an associated GW signal that could be detectable at LISA ($\text{SNR} \geq 1$, see text for details). The characteristics of the light-gray points can be inferred from the left panel. Also shown in both plots is the current limit on κ_λ from ATLAS as well as the projected sensitivities of the HL-LHC and the ILC running at a c.m. energy of 500 GeV.

The value of κ_λ can be experimentally constrained via information from double Higgs boson production at colliders (and indirectly via measurements of single Higgs boson production). In order to compare the 2HDM predictions for κ_λ with present and projected future experimental constraints, we show in Fig. 11 the currently strongest 95% C.L. experimental limit on κ_λ , corresponding to $\kappa_\lambda < 6.3$ as reported by ATLAS¹⁹ using the full Run II dataset and combining measurements of single Higgs boson and (non-resonant) Higgs boson pair production [4]. We also show the projected 95% C.L. sensitivity of the HL-LHC (dashed red line), given by $\kappa_\lambda < 2.2$ [137], and the projected 95% C.L. sensitivity of the future International Linear Collider (ILC) with $\sqrt{s} = 500$ GeV and an integrated luminosity of 4000 fb^{-1} (dashed orange line), given by $\kappa_\lambda < 1.54$ [138]. We stress that the current experimental limits on κ_λ hold under the assumption that the couplings of h to other SM particles are those of the SM, which is the case in the alignment limit of the 2HDM (at leading order) used in this work. In addition, the projected limits shown for the HL-LHC and the ILC assume that $\kappa_\lambda = 1$ will be measured experimentally (we discuss below the consequences if a different value of κ_λ is realized in nature).²⁰ While the current experimental sensitivity at the LHC is not sufficient to probe the viable parameter space analyzed here, the HL-LHC is expected to be capable of probing essentially the entire parameter space featuring EW SnR, and the ILC-

¹⁹CMS has reported a comparable upper limit of $\kappa_\lambda < 6.49$ [3].

²⁰It should be noted that, with our definition of κ_λ (which matches that of the ATLAS and CMS experimental collaborations), $\kappa_\lambda = 1$ corresponds to the SM prediction only if one-loop corrections to λ_{hhh} in the SM (which amount to -9% of the tree-level value [30]) are neglected.

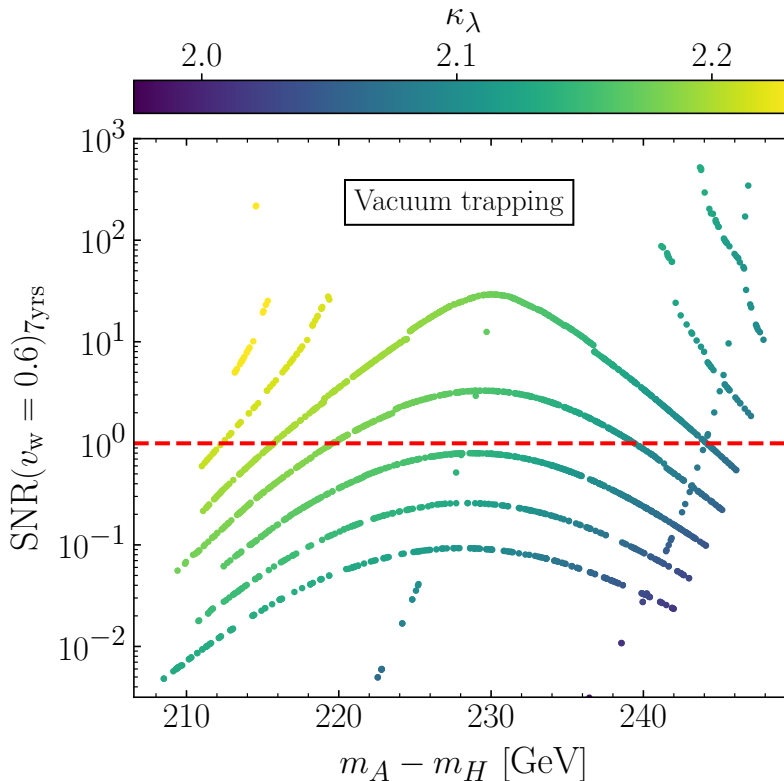


Figure 12: Parameter points of the detailed finer scan discussed in section 4.2.2 (as shown in Fig. 6 and Fig. 9), in the $(\Delta m = m_A - m_H, \text{SNR})$ plane. The color-coding here indicates the prediction for κ_λ .

500 would furthermore probe most of the region featuring a strong FOEWPT, in particular the entire region with a GW signal that could be detectable at LISA (see below).

In order to estimate the values of κ_λ for parameter points with detectable GW signals at LISA, we show in the right panel of Fig. 11 the same parameter plane as in the left panel, but with the strong FOEWPT parameter points predicting $\text{SNR} \geq 1$ at LISA highlighted in light-pink. These points have values of $\kappa_\lambda \sim 2$, and thus lie near the expected HL-LHC upper limit on κ_λ and within the reach of the ILC running at 500 GeV.

To further scrutinize this parameter region, focusing on the interplay between measurements of the Higgs boson self-coupling at colliders and potential observations of GWs at LISA, we show in Fig. 12 the same plane as depicted in Fig. 6 and Fig. 9, with the color-coding now indicating the values of κ_λ (points above the dashed red line in Fig. 12 therefore correspond to the pink area in the right plot of Fig. 11). The predicted values of κ_λ in this plot range from $\kappa_\lambda \sim 2$ up to $\kappa_\lambda \sim 2.2$, possibly within reach of the HL-LHC. The plot furthermore illustrates that a strong FOEWPT that gives rise to a potentially detectable GW signal is associated with a significant deviation from $\kappa_\lambda = 1$ (see also Ref. [32]). Conversely, if no deviations of κ_λ from the SM prediction are observed at the HL-LHC and / or a future e^+e^- Linear Collider running at 500 GeV, no GW signal at LISA would be expected in the considered scenarios.

We also stress that future measurements of κ_λ at the HL-LHC and the ILC will be a very important probe of the EW phase transition, independently of the associated GW production (as shown in Fig. 11, a large fraction of the parameter space featuring a strong FOEWPT does not yield an observable GW signal at LISA). We note in this context that the leading two-loop corrections to the self-coupling of the SM-like Higgs boson can yield a sizable enhancement of

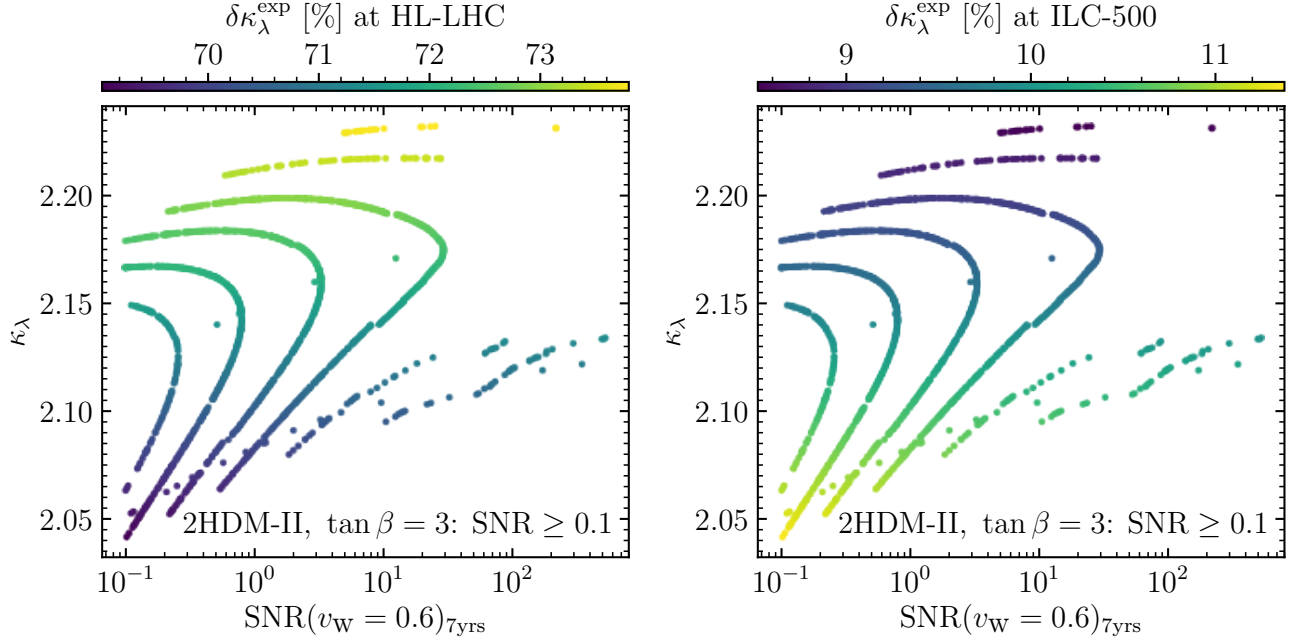


Figure 13: Parameter points from Fig. 12 with $\text{SNR} \geq 0.1$ in the $(\text{SNR}, \kappa_\lambda)$ plane. The color coding of the points indicates the projected experimental precision of the measurement of κ_λ at the HL-LHC (left) and the ILC-500 (right), see text for details.

κ_λ [136] with respect to the one-loop result. Thus, an analysis of κ_λ at the two-loop level may result in even better prospects for a measurement of a modification of the Higgs boson self-coupling with respect to the SM value. We leave such a study for the future.

In all the above discussion, we have focused on the potential of HL-LHC and ILC constraints on κ_λ to exclude the presence of sizable BSM contributions to λ_{hhh} by assuming that the value of $\kappa_\lambda = 1$ is realized in nature. However, as explained above the parameter region of the 2HDM giving rise to a FOEWPT predicts values of κ_λ that are significantly larger than the SM value. Therefore it is also important to assess the capabilities of the HL-LHC and the ILC (or another e^+e^- Linear Collider running at 500 GeV) for making a measurement of the trilinear Higgs boson coupling for the case where $\kappa_\lambda \neq 1$. In fact, the expected HL-LHC and ILC precision of the κ_λ measurement, $\delta\kappa_\lambda^{\text{exp}}$, would significantly change for the case where the true value of κ_λ is above 1 (for $\kappa_\lambda = 1$ the projected HL-LHC and ILC-500 precisions are given by $\delta\kappa_\lambda^{\text{exp}} = 60\%$ [137] and $\delta\kappa_\lambda^{\text{exp}} = 27\%$ [138], respectively). In order to analyze how precisely the HL-LHC and the ILC could measure a value of κ_λ in the 2HDM parameter space region yielding an observable GW signal at LISA, we show in Fig. 13 the parameter points of Fig. 12 with $\text{SNR} \geq 0.1$ in the $(\text{SNR}, \kappa_\lambda)$ plane, with the color-coding indicating the experimental precision with which κ_λ could be measured at the HL-LHC (left panel) and the ILC-500 (right panel). At the HL-LHC, the experimental precision of a $\kappa_\lambda \sim 2$ measurement ($\delta\kappa_\lambda^{\text{exp}} \gtrsim 70\%$) worsens compared to that of $\kappa_\lambda = 1$. This is due to the enhanced destructive interference between the contributions involving and not involving the trilinear Higgs coupling, leading to a reduced cross section at the HL-LHC (see, for instance, Fig. 3 of Ref. [139] for the cross-section predictions). On the other hand, the situation would be much more favorable at the ILC with $\sqrt{s} = 500$ GeV in the process $e^+e^- \rightarrow Zh\bar{h}$, for which a precision of $\delta\kappa_\lambda^{\text{exp}} \sim 10\%$ could be expected for a $\kappa_\lambda \sim 2$ measurement with an integrated luminosity of 4000 fb^{-1} [138]. The Higgs boson self-coupling measurement at the ILC-500 relies mainly on the Higgs-strahlung channel, which exhibits a constructive interference between the different contributions and thus

an enhanced di-Higgs production cross section for $\kappa_\lambda > 1$ (see Fig. 8 of Ref. [140]).

Regarding the interpretation of Fig. 13 we would like to remind the reader that the current theoretical uncertainties on the prediction for the GW spectra from a FOEWPT, as well as the lack of knowledge of the value of v_w (see section 3.5 for details), translate into an uncertainty on the SNR (not shown in the plots) that is much larger than the one that is induced by a collider measurement of the trilinear Higgs coupling with an uncertainty of $\delta\kappa_\lambda^{\text{exp}} \sim 10\%$ (reachable at the ILC-500). Thus, a measurement of $\kappa_\lambda \sim 2$, which would be possible only with rather large uncertainty at the HL-LHC but with a much better precision at the ILC-500 or other e^+e^- colliders running at a similar energy, together with a non-observation of a GW signal at LISA clearly would not rule out a 2HDM (type II) interpretation. On the other hand, if a value of $\kappa_\lambda \sim 1$ is established via collider measurements and a GW signal at LISA is detected, an interpretation within the 2HDM would be strongly disfavored.

5 Conclusions

In this paper we have analyzed the thermal history of the 2HDM, focusing on its type II variant, and its associated phenomenological imprints. It is well known that the 2HDM (in contrast to the SM) can accommodate a strong first-order electroweak phase transition (FOEWPT). The FOEWPT can lead to the production of a primordial gravitational wave (GW) background that could potentially be detectable by the future LISA observatory, and/or allow for the required out-of-equilibrium conditions in order to realize successful baryogenesis. We have shown that the 2HDM may also give rise to other phenomena during its thermal evolution in the early Universe, characterized by vacuum trapping (the Universe remains in an unbroken EW phase, although the EW vacuum is the deepest one at $T = 0$) and EW symmetry non-restoration (SnR), the possibility that the vacuum adopted at high temperature is not the EW symmetric one. Within a simple scenario characterized by the alignment limit ($c_{\beta-\alpha} = 0$) and equal masses for the neutral CP-odd and charged BSM scalars ($m_A = m_{H^\pm}$), we have categorized the different thermal histories which are possible in the (m_H, m_A) plane of the 2HDM: A) the Universe always stays in the EW vacuum (SnR), although at $T = 0$ the EW broken phase is meta-stable; B) the Universe always remains at the EW symmetric state even though a meta-stable (with a lifetime longer than the age of the Universe) EW broken minimum is present at $T = 0$; C) the Universe always remains in the EW broken phase (SnR), which is always the deepest minimum of the potential; D) the Universe always remains in the EW symmetric phase, although at $T = 0$ the EW vacuum is the deepest one (vacuum trapping); E) the Universe undergoes a strong FOEWPT (from the EW symmetric to the broken phase); F) the Universe undergoes a weak first-order or a second-order transition (from the EW symmetric to the broken phase). The fact that regions B and D are unphysical allowed us to determine new limits on the 2HDM parameter space. In particular, regarding the occurrence of vacuum trapping (region D), we have demonstrated that it excludes a sizable region of parameter space that would otherwise feature a strong FOEWPT, stressing the importance of the determination of the false vacuum decay rate and the nucleation temperature at which the EW phase transition does take place. Merely relying on the presence of a critical temperature at which the co-existing EW symmetric and EW broken vacua are equally deep (as frequently applied in the literature, not accounting for vacuum trapping) erroneously assigns the strongest FOEWPTs to regions of the 2HDM parameter space in which actually no transition can occur.

Focusing our analysis on the (type II) 2HDM parameter region featuring a strong FOEWPT, we have found that, even with most optimistic assumptions (bubble-wall velocity $v_w = 0.6$, taking

into account the turbulent motion of the primordial plasma as source for GWs, and $\mathcal{T} = 7$ years of effective LISA observation time), GW signals from the EW epoch that are potentially observable by LISA (with a signal-to-noise ratio $\text{SNR} > 1$) only occur in a very narrow region of the (m_H, m_A) mass plane of the 2HDM, corresponding to very specific values of the mass-splitting $m_A - m_H$ (which are generally large, $200 \text{ GeV} \lesssim m_A - m_H \lesssim 250 \text{ GeV}$) as a function of m_H . Parameter regions with larger mass splittings either feature SnR (and so do not give rise to a FOEWPT) or are unphysical. Indeed, we found that the parameter region giving rise to the strongest GW signals is adjacent to the (unphysical) parameter region featuring vacuum trapping, and we demonstrated that this fact gives rise to the very strong dependence of the amplitude and peak frequency of the potentially detectable GW signals on the underlying model parameters.

In addition, we have explored the collider phenomenology of 2HDM parameter regions yielding a strong FOEWPT, including those generating a GW signal that could be within the future reach of LISA, in order to assess the interplay between the LHC, LISA and future colliders like the ILC to scrutinize FOEWPT scenarios in the 2HDM. First, based on the RGE evolution of 2HDM quartic scalar couplings, the existence of new strongly-coupled physics (beyond the 2HDM) would be needed at energy scales $\Lambda_{4\pi} \sim 1 - 2 \text{ TeV}$ for scenarios yielding an observable GW signal at LISA. We can thus safely argue that such scenarios should be within reach of the (HL-)LHC. At the same time, we have demonstrated that the 2HDM parameter regions that LISA could probe would yield an LHC “smoking gun signature” $pp \rightarrow A \rightarrow ZH, H \rightarrow t\bar{t}$. A conservative extrapolation of the public preliminary results in this channel by the CMS collaboration to HL-LHC integrated luminosities shows that this search would cover essentially the entire region that could be observable by LISA. Again, this has a crucial impact on the possible interplay between LISA and the LHC: the absence of new-physics indications at the (HL-)LHC would make the observation of a GW signal from a FOEWPT in the 2HDM by LISA virtually impossible.

As a final step of our analysis we focussed on the trilinear self-coupling of the Higgs boson at about 125 GeV , λ_{hhh} . We pointed out that the measurement of this coupling constitutes an important probe of a FOEWPT in the early Universe, since FOEWPT scenarios are generically associated with sizable enhancements of λ_{hhh} with respect to its SM value. We have found that regions in the 2HDM parameter space that give rise to GW signals with sizable signal-to-noise ratios at LISA ($\text{SNR} > 0.1$) are associated with large values of $\kappa_\lambda = \lambda_{hhh}/\lambda_{hhh}^{\text{SM}} \sim 2$, and even larger values of κ_λ are found for SnR scenarios. If $\kappa_\lambda \sim 1$ (as in the SM) is realized in nature, $\kappa_\lambda \sim 2$ values are at the border of the 95% C.L. upper limits expected from the measurement of the non-resonant Higgs-boson pair-production at the HL-LHC. Then, SnR scenarios in the 2HDM will be well-probed by this measurement, which will also access the 2HDM parameter region yielding the strongest GW signals. If on the other hand indeed a value of $\kappa_\lambda \sim 2$ is realized in nature, it is important to note that the precision with which κ_λ can be measured significantly depends on its precise value. A value of $\kappa_\lambda \sim 2$ leads to a reduced sensitivity at the HL-LHC, with a precision of only $\sim 70\%$ (compared to $\sim 60\%$ for $\kappa_\lambda \sim 1$) due to the enhanced destructive interference of contributions involving and not involving the trilinear Higgs coupling, leading to a reduced Higgs boson pair production cross section. The situation is reversed at the ILC operating at $\sqrt{s} = 500 \text{ GeV}$: for $\kappa_\lambda = 1$ a $\sim 27\%$ precision on the measurement is anticipated, while for $\kappa_\lambda \sim 2$ the precision increases to $\sim 10\%$ due to an enhanced constructive interference between the different contributions. Since a FOEWPT is naturally connected to values of $\kappa_\lambda > 1$, the general prospects in this case for the HL-LHC to measure the Higgs boson self-coupling are worse than in the SM, whereas they improve substantially for the ILC.

Accordingly, a collider measurement of $\kappa_\lambda \sim 2$, would be well compatible with a 2HDM (type II) interpretation, independently of whether or not a GW signal at LISA will be detected. On the

other hand, a collider measurement of $\kappa_\lambda \sim 1$ together with a GW signal at LISA would strongly disfavor an interpretation within the type II 2HDM.

Acknowledgements

We thank Daniel Hundhausen and Matthias Schröder from the CMS Group at the University of Hamburg for interesting discussions. We are also grateful to Jenny List for the projections of the HL-LHC and ILC sensitivities to the triple Higgs coupling measurements. T.B., M.O.O.R. and G.W. acknowledge support by the Deutsche Forschungsgemeinschaft (DFG, German Research Foundation) under Germany’s Excellence Strategy – EXC 2121 “Quantum Universe” – 390833306. This work has been partially funded by the Deutsche Forschungsgemeinschaft (DFG, German Research Foundation) - 491245950. S.H and J.M.N. acknowledge support from the grant IFT Centro de Excelencia Severo Ochoa CEX2020-001007-S funded by MCIN/AEI/10.13039/501100011033. The work of S.H. was supported in part by the grant PID2019-110058GB-C21 funded by MCIN/AEI/10.13039/501100011033 and by “ERDF A way of making Europe”. The work of J.M.N. was supported by the Ramón y Cajal Fellowship contract RYC-2017-22986, and by grant PGC2018-096646-A-I00 from the Spanish Proyectos de I+D de Generación de Conocimiento. J.M.N. also acknowledges support from the European Union’s Horizon 2020 research and innovation programme under the Marie Skłodowska-Curie grant agreement 860881 (ITN HIDDEN).

A Comparison of the renormalization scale dependence with changes of the 2HDM parameters

In Sect. 2.2 we discussed the impact of the renormalization scale dependence of the effective potential on the predicted values for the quantities that characterize the FOEWPT. We pointed out that the μ -dependence is much smaller compared to the large dependence on the values of the model parameters. In Sect. 4.2.2 it was shown that the dependence on the model parameters is particularly large in the parameter space regions that could potentially feature a FOEWPT that is sufficiently strong to give rise to a detectable GW signal. As a consequence, different choices for the renormalization scale μ (within a physically reasonable range) would not have a major impact on the prospects for a detectable GW signal in certain regions of the 2HDM parameter space.

In order to illustrate this, we show in Fig. 14 the predictions for the LISA SNR of the GW signals in an example scenario taken from the scan discussed in Sect. 4.1. The 2HDM parameters are set as shown in Eq. (34), but for a fixed value of $m_H = 373$ GeV, and the masses $m_A = m_{H^\pm}$ are varied in the small range in which potentially observable GW signals are predicted. We depict the SNR as a function of $m_A = m_{H^\pm}$ for three different values of the renormalization scale: $\mu = v, v/2$ and $2v$ indicated in blue, orange and green, respectively. One can make several observations that demonstrate the robustness of our conclusions with respect to the theoretical uncertainties stemming from the renormalization scale dependence:

(i) Apart from a very small range of mass values, the predicted SNRs of all three curves are orders of magnitudes below 1, indicating that those predicted GW signals would not be observable at LISA, independently of the choice for the renormalization scale μ . Therefore, our conclusions that potentially detectable GW signals only occur in very narrow regions of the analyzed (m_H, m_A) mass plane do not depend on the precise value of μ .

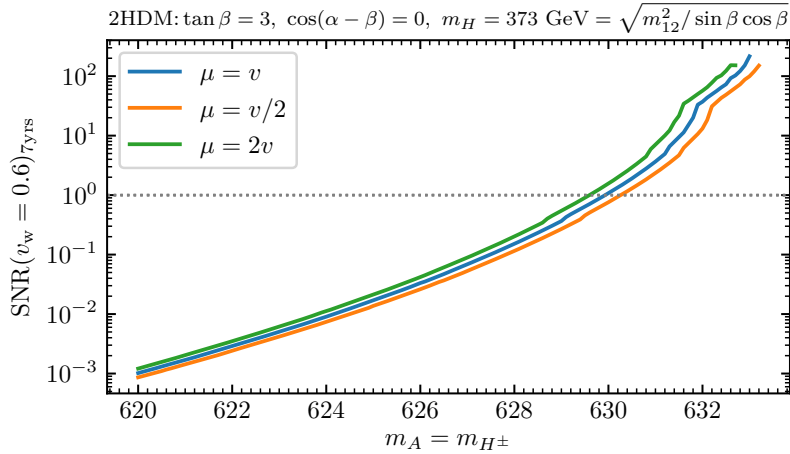


Figure 14: LISA SNR of the GW signal as a function of $m_A = m_{H^\pm}$ (all other parameters are kept fixed) for an example scenario of the scan discussed in Sect. 4.1 for three different choices of the renormalization scale μ .

(ii) For the mass ranges in which the predicted SNRs are of the order of 1 or larger, indicating that the corresponding parameter space regions could potentially be probed with LISA, we find that the variation of μ gives rise to variations of the SNRs by about an order of magnitude. However, the same variation of the SNRs occurs (for a fixed value of μ) if $m_A = m_{H^\pm}$ is varied by less than 1 GeV. This can be seen, for example, by comparing the values of $m_A = m_{H^\pm}$ at which the three colored lines cross the horizontal dashed gray line at $\text{SNR} = 1$. This value changes from $m_A = m_{H^\pm} = 629.5$ GeV for $\mu = v/2$ to $m_A = m_{H^\pm} = 630.0$ GeV for $\mu = 2v$. As a consequence, the minimum amount of the mass splittings between H and A, H^\pm that is required for a sufficiently strong GW signal is only marginally affected by the variation of μ .

(iii) The three colored lines end at a maximum value of $m_A = m_{H^\pm}$ as a consequence of vacuum trapping (see the discussion in Sect. 3.3). The endpoints of the three lines lie within a range of less than 1 GeV in $m_A = m_{H^\pm}$, such that also the maximal mass splitting between H and A, H^\pm that can be realized without the occurrence of vacuum trapping is not significantly affected by the variation of μ .

In summary, our conclusions about the interplay between collider physics at the (HL-)LHC and the possible observation of GW signals at LISA in the context of the type II 2HDM are robust against the uncertainties from the renormalization scale dependence of the effective potential.

References

- [1] ATLAS collaboration, *Observation of a new particle in the search for the Standard Model Higgs boson with the ATLAS detector at the LHC*, *Phys. Lett. B* **716** (2012) 1 [1207.7214].
- [2] CMS collaboration, *Observation of a New Boson at a Mass of 125 GeV with the CMS Experiment at the LHC*, *Phys. Lett. B* **716** (2012) 30 [1207.7235].
- [3] CMS collaboration, *A portrait of the Higgs boson by the CMS experiment ten years after the discovery*, *Nature* **607** (2022) 60 [2207.00043].
- [4] ATLAS collaboration, *Constraining the Higgs boson self-coupling from single- and double-Higgs production with the ATLAS detector using pp collisions at $\sqrt{s} = 13$ TeV*, Tech. Rep. ATLAS-CONF-2022-050 (Jul, 2022).

- [5] P. Huet and E. Sather, *Electroweak baryogenesis and standard model CP violation*, *Phys. Rev. D* **51** (1995) 379 [[hep-ph/9404302](#)].
- [6] M.B. Gavela, M. Lozano, J. Orloff and O. Pene, *Standard model CP violation and baryon asymmetry. Part 1: Zero temperature*, *Nucl. Phys. B* **430** (1994) 345 [[hep-ph/9406288](#)].
- [7] M.B. Gavela, P. Hernandez, J. Orloff, O. Pene and C. Quimbay, *Standard model CP violation and baryon asymmetry. Part 2: Finite temperature*, *Nucl. Phys. B* **430** (1994) 382 [[hep-ph/9406289](#)].
- [8] K. Kajantie, M. Laine, K. Rummukainen and M.E. Shaposhnikov, *Is there a hot electroweak phase transition at $m(H)$ larger or equal to $m(W)$?*, *Phys. Rev. Lett.* **77** (1996) 2887 [[hep-ph/9605288](#)].
- [9] T.D. Lee, *A Theory of Spontaneous T Violation*, *Phys. Rev. D* **8** (1973) 1226.
- [10] J.E. Kim, *Weak Interaction Singlet and Strong CP Invariance*, *Phys. Rev. Lett.* **43** (1979) 103.
- [11] F. Wilczek, *Problem of Strong P and T Invariance in the Presence of Instantons*, *Phys. Rev. Lett.* **40** (1978) 279.
- [12] J.M. Cline and P.-A. Lemieux, *Electroweak phase transition in two Higgs doublet models*, *Phys. Rev. D* **55** (1997) 3873 [[hep-ph/9609240](#)].
- [13] L. Fromme, S.J. Huber and M. Seniuch, *Baryogenesis in the two-Higgs doublet model*, *JHEP* **11** (2006) 038 [[hep-ph/0605242](#)].
- [14] J.M. Cline, K. Kainulainen and M. Trott, *Electroweak Baryogenesis in Two Higgs Doublet Models and B meson anomalies*, *JHEP* **11** (2011) 089 [[1107.3559](#)].
- [15] G. Dorsch, S. Huber, T. Konstandin and J. No, *A Second Higgs Doublet in the Early Universe: Baryogenesis and Gravitational Waves*, *JCAP* **05** (2017) 052 [[1611.05874](#)].
- [16] A.G. Cohen, D.B. Kaplan and A.E. Nelson, *Progress in electroweak baryogenesis*, *Ann. Rev. Nucl. Part. Sci.* **43** (1993) 27 [[hep-ph/9302210](#)].
- [17] M. Trodden, *Electroweak baryogenesis*, *Rev. Mod. Phys.* **71** (1999) 1463 [[hep-ph/9803479](#)].
- [18] D.E. Morrissey and M.J. Ramsey-Musolf, *Electroweak baryogenesis*, *New J. Phys.* **14** (2012) 125003 [[1206.2942](#)].
- [19] A.D. Sakharov, *Violation of CP Invariance, C asymmetry, and baryon asymmetry of the universe*, *Pisma Zh. Eksp. Teor. Fiz.* **5** (1967) 32.
- [20] C. Caprini et al., *Detecting gravitational waves from cosmological phase transitions with LISA: an update*, *JCAP* **03** (2020) 024 [[1910.13125](#)].
- [21] P. Auclair et al., *Cosmology with the Laser Interferometer Space Antenna*, [2204.05434](#).
- [22] S. Weinberg, *Gauge and Global Symmetries at High Temperature*, *Phys. Rev. D* **9** (1974) 3357.
- [23] J.M. Cline, G.D. Moore and G. Servant, *Was the electroweak phase transition preceded by a color broken phase?*, *Phys. Rev. D* **60** (1999) 105035 [[hep-ph/9902220](#)].
- [24] S. Baum, M. Carena, N.R. Shah, C.E. Wagner and Y. Wang, *Nucleation is More than Critical – A Case Study of the Electroweak Phase Transition in the NMSSM*, [2009.10743](#).
- [25] T. Biekötter, S. Heinemeyer, J.M. No, M.O. Olea and G. Weiglein, *Fate of electroweak symmetry in the early Universe: Non-restoration and trapped vacua in the $N2HDM$* , *JCAP* **06** (2021) 018 [[2103.12707](#)].
- [26] G. Branco, P. Ferreira, L. Lavoura, M. Rebelo, M. Sher and J.P. Silva, *Theory and phenomenology of two-Higgs-doublet models*, *Phys. Rept.* **516** (2012) 1 [[1106.0034](#)].
- [27] G. Dorsch, S. Huber and J. No, *A strong electroweak phase transition in the 2HDM after LHC8*, *JHEP* **10** (2013) 029 [[1305.6610](#)].
- [28] G. Dorsch, S. Huber, K. Mimasu and J. No, *Echoes of the Electroweak Phase Transition: Discovering a second Higgs doublet through $A_0 \rightarrow ZH_0$* , *Phys. Rev. Lett.* **113** (2014) 211802 [[1405.5537](#)].
- [29] P. Basler, M. Krause, M. Muhlleitner, J. Wittbrodt and A. Wlotzka, *Strong First Order Electroweak Phase Transition in the CP-Conserving 2HDM Revisited*, *JHEP* **02** (2017) 121 [[1612.04086](#)].
- [30] G. Dorsch, S. Huber, K. Mimasu and J. No, *The Higgs Vacuum Uplifted: Revisiting the Electroweak Phase Transition with a Second Higgs Doublet*, *JHEP* **12** (2017) 086 [[1705.09186](#)].

- [31] J. Bernon, L. Bian and Y. Jiang, *A new insight into the phase transition in the early Universe with two Higgs doublets*, *JHEP* **05** (2018) 151 [[1712.08430](#)].
- [32] D. Gonçalves, A. Kaladharan and Y. Wu, *Electroweak phase transition in the 2HDM: collider and gravitational wave complementarity*, [2108.05356](#).
- [33] A. Noble and M. Perelstein, *Higgs self-coupling as a probe of electroweak phase transition*, *Phys. Rev. D* **78** (2008) 063518 [[0711.3018](#)].
- [34] P. Huang, A. Joglekar, B. Li and C.E.M. Wagner, *Probing the Electroweak Phase Transition at the LHC*, *Phys. Rev. D* **93** (2016) 055049 [[1512.00068](#)].
- [35] J.F. Gunion and H.E. Haber, *The CP conserving two Higgs doublet model: The Approach to the decoupling limit*, *Phys. Rev. D* **67** (2003) 075019 [[hep-ph/0207010](#)].
- [36] R. Coimbra, M.O. Sampaio and R. Santos, *ScannerS: Constraining the phase diagram of a complex scalar singlet at the LHC*, *Eur. Phys. J. C* **73** (2013) 2428 [[1301.2599](#)].
- [37] M. Mühlleitner, M.O. Sampaio, R. Santos and J. Wittbrodt, *ScannerS: Parameter Scans in Extended Scalar Sectors*, [2007.02985](#).
- [38] J. Haller, A. Hoecker, R. Kogler, K. Mönig, T. Peiffer and J. Stelzer, *Update of the global electroweak fit and constraints on two-Higgs-doublet models*, *Eur. Phys. J. C* **78** (2018) 675 [[1803.01853](#)].
- [39] W. Grimus, L. Lavoura, O. Ogreid and P. Osland, *A Precision constraint on multi-Higgs-doublet models*, *J. Phys. G* **35** (2008) 075001 [[0711.4022](#)].
- [40] W. Grimus, L. Lavoura, O. Ogreid and P. Osland, *The Oblique parameters in multi-Higgs-doublet models*, *Nucl. Phys. B* **801** (2008) 81 [[0802.4353](#)].
- [41] CDF collaboration, *High-precision measurement of the W boson mass with the CDF II detector*, *Science* **376** (2022) 170.
- [42] P. Bechtle, S. Heinemeyer, O. Stål, T. Stefaniak and G. Weiglein, *HiggsSignals: Confronting arbitrary Higgs sectors with measurements at the Tevatron and the LHC*, *Eur. Phys. J. C* **74** (2014) 2711 [[1305.1933](#)].
- [43] O. Stål and T. Stefaniak, *Constraining extended Higgs sectors with HiggsSignals*, *PoS EPS-HEP2013* (2013) 314 [[1310.4039](#)].
- [44] P. Bechtle, S. Heinemeyer, O. Stål, T. Stefaniak and G. Weiglein, *Probing the Standard Model with Higgs signal rates from the Tevatron, the LHC and a future ILC*, *JHEP* **11** (2014) 039 [[1403.1582](#)].
- [45] P. Bechtle, S. Heinemeyer, T. Klingl, T. Stefaniak, G. Weiglein and J. Wittbrodt, *HiggsSignals-2: Probing new physics with precision Higgs measurements in the LHC 13 TeV era*, [2012.09197](#).
- [46] P. Bechtle, O. Brein, S. Heinemeyer, G. Weiglein and K.E. Williams, *HiggsBounds: Confronting Arbitrary Higgs Sectors with Exclusion Bounds from LEP and the Tevatron*, *Comput. Phys. Commun.* **181** (2010) 138 [[0811.4169](#)].
- [47] P. Bechtle, O. Brein, S. Heinemeyer, G. Weiglein and K.E. Williams, *HiggsBounds 2.0.0: Confronting Neutral and Charged Higgs Sector Predictions with Exclusion Bounds from LEP and the Tevatron*, *Comput. Phys. Commun.* **182** (2011) 2605 [[1102.1898](#)].
- [48] P. Bechtle, O. Brein, S. Heinemeyer, O. Stål, T. Stefaniak, G. Weiglein et al., *Recent Developments in HiggsBounds and a Preview of HiggsSignals*, *PoS CHARGED2012* (2012) 024 [[1301.2345](#)].
- [49] P. Bechtle, O. Brein, S. Heinemeyer, O. Stål, T. Stefaniak, G. Weiglein et al., *HiggsBounds – 4: Improved Tests of Extended Higgs Sectors against Exclusion Bounds from LEP, the Tevatron and the LHC*, *Eur. Phys. J. C* **74** (2014) 2693 [[1311.0055](#)].
- [50] P. Bechtle, D. Dercks, S. Heinemeyer, T. Klingl, T. Stefaniak, G. Weiglein et al., *HiggsBounds-5: Testing Higgs Sectors in the LHC 13 TeV Era*, *Eur. Phys. J. C* **80** (2020) 1211 [[2006.06007](#)].
- [51] R.V. Harlander, S. Liebler and H. Mantler, *SusHi: A program for the calculation of Higgs production in gluon fusion and bottom-quark annihilation in the Standard Model and the MSSM*, *Comput. Phys. Commun.* **184** (2013) 1605 [[1212.3249](#)].
- [52] I. Engeln, M. Mühlleitner and J. Wittbrodt, *N2HDECAY: Higgs Boson Decays in the Different Phases of the N2HDM*, *Comput. Phys. Commun.* **234** (2019) 256 [[1805.00966](#)].

- [53] M. Quiros, *Finite temperature field theory and phase transitions*, in *ICTP Summer School in High-Energy Physics and Cosmology*, pp. 187–259, 1, 1999 [[hep-ph/9901312](#)].
- [54] S.R. Coleman and E.J. Weinberg, *Radiative Corrections as the Origin of Spontaneous Symmetry Breaking*, *Phys. Rev. D* **7** (1973) 1888.
- [55] L. Dolan and R. Jackiw, *Symmetry Behavior at Finite Temperature*, *Phys. Rev. D* **9** (1974) 3320.
- [56] H.H. Patel and M.J. Ramsey-Musolf, *Baryon Washout, Electroweak Phase Transition, and Perturbation Theory*, *JHEP* **07** (2011) 029 [[1101.4665](#)].
- [57] C. Wainwright, S. Profumo and M.J. Ramsey-Musolf, *Gravity Waves from a Cosmological Phase Transition: Gauge Artifacts and Daisy Resummations*, *Phys. Rev. D* **84** (2011) 023521 [[1104.5487](#)].
- [58] M. Garny and T. Konstandin, *On the gauge dependence of vacuum transitions at finite temperature*, *JHEP* **07** (2012) 189 [[1205.3392](#)].
- [59] P. Basler and M. Mühlleitner, *BSMPT (Beyond the Standard Model Phase Transitions): A tool for the electroweak phase transition in extended Higgs sectors*, *Comput. Phys. Commun.* **237** (2019) 62 [[1803.02846](#)].
- [60] P. Basler, M. Mühlleitner and J. Müller, *BSMPT v2 A Tool for the Electroweak Phase Transition and the Baryon Asymmetry of the Universe in Extended Higgs Sectors*, [2007.01725](#).
- [61] D. Croon, O. Gould, P. Schicho, T.V.I. Tenkanen and G. White, *Theoretical uncertainties for cosmological first-order phase transitions*, *JHEP* **04** (2021) 055 [[2009.10080](#)].
- [62] J. Oredsson, *2HDME : Two-Higgs-Doublet Model Evolver*, *Comput. Phys. Commun.* **244** (2019) 409 [[1811.08215](#)].
- [63] M. Carena, C. Krause, Z. Liu and Y. Wang, *New approach to electroweak symmetry nonrestoration*, *Phys. Rev. D* **104** (2021) 055016 [[2104.00638](#)].
- [64] D.J. Gross, R.D. Pisarski and L.G. Yaffe, *QCD and Instantons at Finite Temperature*, *Rev. Mod. Phys.* **53** (1981) 43.
- [65] R.R. Parwani, *Resummation in a hot scalar field theory*, *Phys. Rev. D* **45** (1992) 4695 [[hep-ph/9204216](#)].
- [66] P.B. Arnold and O. Espinosa, *The Effective potential and first order phase transitions: Beyond leading-order*, *Phys. Rev. D* **47** (1993) 3546 [[hep-ph/9212235](#)].
- [67] P. Schicho, T.V.I. Tenkanen and G. White, *Combining thermal resummation and gauge invariance for electroweak phase transition*, [2203.04284](#).
- [68] M. Carrington, *The Effective potential at finite temperature in the Standard Model*, *Phys. Rev. D* **45** (1992) 2933.
- [69] C.L. Wainwright, *CosmoTransitions: Computing Cosmological Phase Transition Temperatures and Bubble Profiles with Multiple Fields*, *Comput. Phys. Commun.* **183** (2012) 2006 [[1109.4189](#)].
- [70] S.R. Coleman, *The Fate of the False Vacuum. 1. Semiclassical Theory*, *Phys. Rev. D* **15** (1977) 2929.
- [71] J. Callan, Curtis G. and S.R. Coleman, *The Fate of the False Vacuum. 2. First Quantum Corrections*, *Phys. Rev. D* **16** (1977) 1762.
- [72] A.D. Linde, *Fate of the False Vacuum at Finite Temperature: Theory and Applications*, *Phys. Lett. B* **100** (1981) 37.
- [73] A.D. Linde, *Decay of the False Vacuum at Finite Temperature*, *Nucl. Phys. B* **216** (1983) 421.
- [74] J. Espinosa, T. Konstandin, J. No and M. Quiros, *Some Cosmological Implications of Hidden Sectors*, *Phys. Rev. D* **78** (2008) 123528 [[0809.3215](#)].
- [75] S. Kanemura and M. Tanaka, *Strongly first-order electroweak phase transition by relatively heavy additional Higgs bosons*, [2201.04791](#).
- [76] F. Giese, T. Konstandin and J. van de Vis, *Model-independent energy budget of cosmological first-order phase transitions—A sound argument to go beyond the bag model*, *JCAP* **07** (2020) 057 [[2004.06995](#)].
- [77] J. Ellis, M. Lewicki and J.M. No, *On the Maximal Strength of a First-Order Electroweak Phase Transition and its Gravitational Wave Signal*, *JCAP* **04** (2019) 003 [[1809.08242](#)].
- [78] D. Bodeker and G.D. Moore, *Can electroweak bubble walls run away?*, *JCAP* **05** (2009) 009 [[0903.4099](#)].

- [79] D. Bodeker and G.D. Moore, *Electroweak Bubble Wall Speed Limit*, *JCAP* **05** (2017) 025 [[1703.08215](#)].
- [80] G.D. Moore and T. Prokopec, *How fast can the wall move? A Study of the electroweak phase transition dynamics*, *Phys. Rev. D* **52** (1995) 7182 [[hep-ph/9506475](#)].
- [81] T. Konstandin, G. Nardini and I. Rues, *From Boltzmann equations to steady wall velocities*, *JCAP* **09** (2014) 028 [[1407.3132](#)].
- [82] J. Kozaczuk, *Bubble Expansion and the Viability of Singlet-Driven Electroweak Baryogenesis*, *JHEP* **10** (2015) 135 [[1506.04741](#)].
- [83] G.C. Dorsch, S.J. Huber and T. Konstandin, *Bubble wall velocities in the Standard Model and beyond*, *JCAP* **12** (2018) 034 [[1809.04907](#)].
- [84] M. Barroso Mancha, T. Prokopec and B. Swiezevska, *Field-theoretic derivation of bubble-wall force*, *JHEP* **01** (2021) 070 [[2005.10875](#)].
- [85] B. Laurent and J.M. Cline, *Fluid equations for fast-moving electroweak bubble walls*, *Phys. Rev. D* **102** (2020) 063516 [[2007.10935](#)].
- [86] G.C. Dorsch, S.J. Huber and T. Konstandin, *A sonic boom in bubble wall friction*, *JCAP* **04** (2022) 010 [[2112.12548](#)].
- [87] W.-Y. Ai, B. Garbrecht and C. Tamarit, *Bubble wall velocities in local equilibrium*, *JCAP* **03** (2022) 015 [[2109.13710](#)].
- [88] M. Lewicki, M. Merchand and M. Zych, *Electroweak bubble wall expansion: gravitational waves and baryogenesis in Standard Model-like thermal plasma*, *JHEP* **02** (2022) 017 [[2111.02393](#)].
- [89] B. Laurent and J.M. Cline, *First principles determination of bubble wall velocity*, *Phys. Rev. D* **106** (2022) 023501 [[2204.13120](#)].
- [90] J.R. Espinosa, M. Losada and A. Riotto, *Symmetry nonrestoration at high temperature in little Higgs models*, *Phys. Rev. D* **72** (2005) 043520 [[hep-ph/0409070](#)].
- [91] P. Meade and H. Ramani, *Unrestored Electroweak Symmetry*, *Phys. Rev. Lett.* **122** (2019) 041802 [[1807.07578](#)].
- [92] I. Baldes and G. Servant, *High scale electroweak phase transition: baryogenesis $\setminus \mathcal{E}$ symmetry non-restoration*, *JHEP* **10** (2018) 053 [[1807.08770](#)].
- [93] A. Glioti, R. Rattazzi and L. Vecchi, *Electroweak Baryogenesis above the Electroweak Scale*, *JHEP* **04** (2019) 027 [[1811.11740](#)].
- [94] O. Matsedonskyi and G. Servant, *High-Temperature Electroweak Symmetry Non-Restoration from New Fermions and Implications for Baryogenesis*, *JHEP* **09** (2020) 012 [[2002.05174](#)].
- [95] M.J. Ramsey-Musolf, P. Winslow and G. White, *Color Breaking Baryogenesis*, *Phys. Rev. D* **97** (2018) 123509 [[1708.07511](#)].
- [96] R. Caldwell et al., *Detection of Early-Universe Gravitational Wave Signatures and Fundamental Physics*, **2203.07972**.
- [97] M. Hindmarsh, S.J. Huber, K. Rummukainen and D.J. Weir, *Shape of the acoustic gravitational wave power spectrum from a first order phase transition*, *Phys. Rev. D* **96** (2017) 103520 [[1704.05871](#)].
- [98] M. Hindmarsh, S.J. Huber, K. Rummukainen and D.J. Weir, *Numerical simulations of acoustically generated gravitational waves at a first order phase transition*, *Phys. Rev. D* **92** (2015) 123009 [[1504.03291](#)].
- [99] M. Hindmarsh, *Sound shell model for acoustic gravitational wave production at a first-order phase transition in the early Universe*, *Phys. Rev. Lett.* **120** (2018) 071301 [[1608.04735](#)].
- [100] M. Hindmarsh and M. Hijazi, *Gravitational waves from first order cosmological phase transitions in the Sound Shell Model*, *JCAP* **12** (2019) 062 [[1909.10040](#)].
- [101] J.R. Espinosa, T. Konstandin, J.M. No and G. Servant, *Energy Budget of Cosmological First-order Phase Transitions*, *JCAP* **06** (2010) 028 [[1004.4187](#)].
- [102] J. Ellis, M. Lewicki and J.M. No, *Gravitational waves from first-order cosmological phase transitions: lifetime of the sound wave source*, *JCAP* **07** (2020) 050 [[2003.07360](#)].

- [103] C. Caprini, R. Durrer and G. Servant, *The stochastic gravitational wave background from turbulence and magnetic fields generated by a first-order phase transition*, *JCAP* **12** (2009) 024 [0909.0622].
- [104] A. Brandenburg, T. Kahniashvili, S. Mandal, A. Roper Pol, A.G. Tevzadze and T. Vachaspati, *Evolution of hydromagnetic turbulence from the electroweak phase transition*, *Phys. Rev. D* **96** (2017) 123528 [1711.03804].
- [105] A. Roper Pol, S. Mandal, A. Brandenburg, T. Kahniashvili and A. Kosowsky, *Numerical simulations of gravitational waves from early-universe turbulence*, *Phys. Rev. D* **102** (2020) 083512 [1903.08585].
- [106] P. Auclair, C. Caprini, D. Cutting, M. Hindmarsh, K. Rummukainen, D.A. Steer et al., *Generation of gravitational waves from freely decaying turbulence*, [2205.02588](#).
- [107] D. Cutting, M. Hindmarsh and D.J. Weir, *Vorticity, kinetic energy, and suppressed gravitational wave production in strong first order phase transitions*, *Phys. Rev. Lett.* **125** (2020) 021302 [1906.00480].
- [108] E. Thrane and J.D. Romano, *Sensitivity curves for searches for gravitational-wave backgrounds*, *Phys. Rev. D* **88** (2013) 124032 [1310.5300].
- [109] LISA collaboration, *Science Requirements Document*, <https://www.cosmos.esa.int/web/lisa/lisa-documents>, Tech. Rep. ESA-L3-EST-SCI-RS-001 (2018).
- [110] M. Aoki, T. Komatsu and H. Shibuya, *Possibility of multi-step electroweak phase transition in the two Higgs doublet models*, [2106.03439](#).
- [111] F. Staub, *Reopen parameter regions in Two-Higgs Doublet Models*, *Phys. Lett. B* **776** (2018) 407 [1705.03677].
- [112] A. Barroso, P.M. Ferreira, I.P. Ivanov and R. Santos, *Metastability bounds on the two Higgs doublet model*, *JHEP* **06** (2013) 045 [1303.5098].
- [113] L. Niemi, M.J. Ramsey-Musolf, T.V.I. Tenkanen and D.J. Weir, *Thermodynamics of a Two-Step Electroweak Phase Transition*, *Phys. Rev. Lett.* **126** (2021) 171802 [2005.11332].
- [114] O. Matsedonskyi, *High-Temperature Electroweak Symmetry Breaking by SM Twins*, *JHEP* **04** (2021) 036 [2008.13725].
- [115] D. Bodeker and W. Buchmuller, *Baryogenesis from the weak scale to the grand unification scale*, *Rev. Mod. Phys.* **93** (2021) 035004 [2009.07294].
- [116] O. Matsedonskyi, J. Unwin and Q. Wang, *Electroweak symmetry non-restoration from dark matter*, *JHEP* **12** (2021) 167 [2107.07560].
- [117] J.M. Cline and K. Kainulainen, *Improved Electroweak Phase Transition with Subdominant Inert Doublet Dark Matter*, *Phys. Rev. D* **87** (2013) 071701 [1302.2614].
- [118] P. Basler, M. Mühlleitner and J. Wittbrodt, *The CP-Violating 2HDM in Light of a Strong First Order Electroweak Phase Transition and Implications for Higgs Pair Production*, *JHEP* **03** (2018) 061 [1711.04097].
- [119] P. Basler, M. Mühlleitner and J. Müller, *Electroweak Phase Transition in Non-Minimal Higgs Sectors*, *JHEP* **05** (2020) 016 [1912.10477].
- [120] S. Fabian, F. Goertz and Y. Jiang, *Dark matter and nature of electroweak phase transition with an inert doublet*, *JCAP* **09** (2021) 011 [2012.12847].
- [121] W. Su, A.G. Williams and M. Zhang, *Strong first order electroweak phase transition in 2HDM confronting future Z & Higgs factories*, *JHEP* **04** (2021) 219 [2011.04540].
- [122] M. Gabelmann, M.M. Mühlleitner and J. Müller, *Electroweak phase transitions with BSM fermions*, *JHEP* **01** (2022) 012 [2107.09617].
- [123] O. Atkinson, M. Black, A. Lenz, A. Rusov and J. Wynne, *Cornering the Two Higgs Doublet Model Type II*, [2107.05650](#).
- [124] O. Atkinson, M. Black, C. Englert, A. Lenz, A. Rusov and J. Wynne, *The Flavourful Present and Future of 2HDMs at the Collider Energy Frontier*, [2202.08807](#).
- [125] L.S. Friedrich, M.J. Ramsey-Musolf, T.V.I. Tenkanen and V.Q. Tran, *Addressing the Gravitational Wave - Collider Inverse Problem*, [2203.05889](#).

- [126] P. Basler, P.M. Ferreira, M. Mühlleitner and R. Santos, *High scale impact in alignment and decoupling in two-Higgs doublet models*, *Phys. Rev. D* **97** (2018) 095024 [[1710.10410](#)].
- [127] CMS collaboration, *Search for neutral resonances decaying into a Z boson and a pair of b jets or τ leptons*, *Phys. Lett. B* **759** (2016) 369 [[1603.02991](#)].
- [128] ATLAS collaboration, *Search for a heavy Higgs boson decaying into a Z boson and another heavy Higgs boson in the $\ell b\bar{b}$ final state in pp collisions at $\sqrt{s} = 13$ TeV with the ATLAS detector*, *Phys. Lett. B* **783** (2018) 392 [[1804.01126](#)].
- [129] CMS collaboration, *Search for new neutral Higgs bosons through the $H \rightarrow ZA \rightarrow \ell^+ \ell^- b\bar{b}$ process in pp collisions at $\sqrt{s} = 13$ TeV*, *JHEP* **03** (2020) 055 [[1911.03781](#)].
- [130] U. Haisch and G. Polesello, *Searching for heavy Higgs bosons in the $t\bar{t}Z$ and tbW final states*, *JHEP* **09** (2018) 151 [[1807.07734](#)].
- [131] D. Gonçalves, A. Kaladharan and Y. Wu, *Resonant top pair searches at the LHC: a window to electroweak phase transition*, [2206.08381](#).
- [132] R. Kuesters, T. Moskalets and S. Argyropoulos, *Search for $A \rightarrow ZH \rightarrow \ell\ell t\bar{t}$ at $\sqrt{2} = 13$ TeV with the ATLAS detector*, *Contribution to: DPG Spring Meeting*, 2022.
- [133] D. Hundhausen, K. De Leo, Y. Fischer, J. Haller and M. Schroeder, *Search for heavy Higgs bosons in the $Z + t\bar{t}$ final state with CMS*, *Contribution to: DPG Spring Meeting*, 2022.
- [134] Y. Fischer, *Search for heavy Higgs bosons in the $Z + t\bar{t}$ final state with the CMS detector*, Master's thesis, Universität Hamburg, 2021.
- [135] A. Ashoorioon and T. Konstandin, *Strong electroweak phase transitions without collider traces*, *JHEP* **07** (2009) 086 [[0904.0353](#)].
- [136] H. Bahl, J. Braathen and G. Weiglein, *New constraints on extended Higgs sectors from the trilinear Higgs coupling*, [2202.03453](#).
- [137] M. Cepeda et al., *Report from Working Group 2: Higgs Physics at the HL-LHC and HE-LHC*, *CERN Yellow Rep. Monogr.* **7** (2019) 221 [[1902.00134](#)].
- [138] C.F. Dürig, *Measuring the Higgs Self-coupling at the International Linear Collider*, Ph.D. thesis, Hamburg U., Hamburg, 2016. [10.3204/PUBDB-2016-04283](#).
- [139] R. Frederix, S. Frixione, V. Hirschi, F. Maltoni, O. Mattelaer, P. Torrielli et al., *Higgs pair production at the LHC with NLO and parton-shower effects*, *Phys. Lett. B* **732** (2014) 142 [[1401.7340](#)].
- [140] LCC PHYSICS WORKING GROUP collaboration, *Tests of the Standard Model at the International Linear Collider*, [1908.11299](#).